nature biomedical engineering

Article

https://doi.org/10.1038/s41551-026-01642-6

Programmable kinetic barcoding for multiplexed RNA detection with Cas13a

Received: 24 April 2025

Accepted: 25 February 2026

Published online: 31 March 2026

Check for updates

Sungmin Son[1,2] ✉, Amy Lyden[1,3], Carlos F. Ng[1,3], Andres Dextre[1,3], Jeffrey Shu[4], Stephanie I. Stephens[4], Parinaz Fozouni[4,5,6,7], Gavin J. Knott[8,9,10], Dylan C. J. Smock[8,9], Tina Y. Liu[8,9,11,12], Daniela Boehm[4], Camille Simoneau[4], G. Renuka Kumar[4], Jennifer A. Doudna[4,8,9,13,14,15,16], Melanie Ott[4,7,17] ✉ & Daniel A. Fletcher[1,3,15,16,17,18] ✉

Rapid identification of viral infections and specific variants in patient samples requires a simple and multiplexed RNA detection method that does not rely on DNA sequencing. Although recent direct detection assays based on CRISPR–Cas13a offer rapid RNA detection by avoiding reverse transcription and DNA amplification required of gold-standard PCR assays, these assays are not easily multiplexed to detect multiple viruses or variants without dividing the sample into separate reactions. Here we show that Cas13a acting on single-target RNAs exhibits variable nuclease activity that depends on the interaction between the target RNA and crRNA. To exploit this feature for multiplexed detection, we devised a crRNA modification strategy that enables programmable tuning of Cas13a's nuclease enzymatic rates. Using a droplet-based Cas13a assay, we demonstrate that kinetic signatures can be harnessed to differentiate among respiratory viruses and SARS-CoV-2 variants in contrived and clinical samples. This kinetic barcoding strategy can be extended to additional RNA targets through simple modification of crRNAs.

Diagnostic testing for viral infections must be rapid and specific to accurately monitor the spread of variants and enable timely responses. In the case of severe acute respiratory syndrome coronavirus 2 (SARS-CoV-2), where symptoms are non-specific and often indistinguishable from other respiratory infections, accurate identification of virus is crucial for optimal and timely treatment[1]. While genomic sequencing provides the most complete information about a virus, a more rapid diagnostic method that can simultaneously detect multiple viral targets and variants is also needed. Although commercial platforms are available that offer multiplexed detection based on PCR reactions[2,3], they typically require complex hardware and long times. Clustered regularly interspaced short palindromic repeats (CRISPR)-associated protein (CRISPR–Cas) systems such as Cas13a offer an alternative method for detecting nucleic acids based on sequence-specific activation[4–6]. Although Cas13 can be combined with reverse transcription, DNA amplification and transcription to increase sensitivity[7,8], we previously demonstrated that Cas13 can avoid limitations associated with those steps and sensitively detect viral RNA without amplification of its gene[4].

Here we show that Cas13-based RNA detection can be multiplexed by quantifying differences in single-enzyme kinetics with a droplet-based version of the Cas13 direct detection assay, where droplet size makes it likely for a maximum of one target RNA to end up in each reaction. This strategy, which we call 'kinetic barcoding', arises from the observation that Cas13 complexed with a single-target RNA exhibits variable nuclease activity depending on the specific CRISPR RNA (crRNA) and target RNA present. This variability is well known from guide screening efforts necessary to identify a subset of 'good' crRNA with high nuclease activity for a given target RNA. We find that such natural differences in kinetics are sufficient to distinguish different viral targets in the droplet Cas13 assay. Moreover, we show that the average enzymatic rate of Cas13 nuclease can be altered in a controlled way by adding single-stranded DNA to the 5′ end of the crRNA. Addition of ten or more deoxynucleotides to the crRNA results in a reproducible

A full list of affiliations appears at the end of the paper. ✉e-mail: smson@kaist.ac.kr; melanie.ott@gladstone.ucsf.edu; fletch@berkeley.edu

and quantifiable stepwise decrease in cleavage rates of fluorophore–quencher molecules used as reporters. By combining multiple crRNAs targeting different viruses or variants that have been modified through the addition of a 5′ DNA sequence to produce distinct activity, the identity of a single-target RNA can be determined solely based on the slope or endpoint value of the fluorescence signal, without the need for separate fluorescence channels. In contrast to other multiplexing strategies that divide samples and then look for different RNA targets in each reaction, kinetic barcoding simultaneously looks for all different RNA targets in all reactions since Cas13 and the barcoded crRNAs are present in all droplets, allowing assay multiplexing without any modifications in the assay workflow or in the hardware.

Results

A droplet Cas13 assay enables single-enzyme kinetics measurements

We first developed a simple and rapid droplet Cas13 assay using emulsification. The small droplet volumes accelerate the accumulation of cleaved fluorophores from reporter molecules (Fig. 1a) in addition to encapsulating single-target RNAs, making it possible to precisely measure single Cas13 enzyme activity. We generated approximately 10 pl droplets by emulsifying a reaction mix containing target RNA, crRNA, fluorophore–quencher reporter and LbuCas13a for 2 min in an excess volume of an oil/surfactant/detergent mixture using an automatic multichannel pipettor and a pipetting robot (Methods, Extended Data Fig. 1a and Supplementary Video 1). We loaded the resulting emulsion, with diameters ranging from 10 µm to 40 µm, into a custom imaging chamber and directly imaged the reaction in time on a fluorescence microscope (Fig. 1b and Extended Data Fig. 1b,c). Imaging the droplets allowed us to normalize the fluorescence signal by droplet size[9], avoiding the need for slower and low-throughput systems for generating uniform droplets.

Accurate determination of enzyme kinetics relies on knowing the active enzyme concentration. In bulk measurements of LbuCas13a kinetics[4], it has been unknown what fraction of target RNA is actually activating LbuCas13a, leading to some debate[10]. In the droplet reaction, by contrast, the active enzyme concentration is known since the fluorescence signal is produced by a single-target RNA activating LbuCas13a. We chose a crRNA targeting the SARS-CoV-2 N gene (crRNA 4) and formed droplets containing crRNA 4 along with SARS-CoV-2 RNA, LbuCas13a and a fluorophore–quencher pair tethered by pentauridine (5U) RNA (reporter) (Fig. 1a). For a target RNA concentration of 1×10^4 copies per µl, we found that 7% of the droplets contain the target RNA, with more than 95% of those containing only a single copy, allowing direct measurement of a single-Cas13a enzyme kinetics. As expected, we found that the signal accumulation rate in positive droplets was inversely proportional to droplet size, with smaller droplets increasing faster than larger droplets (9-fold increase for a 23 µm droplet versus 3-fold increase for a 42 µm droplet) (Fig. 1b–d). We found that a single LbuCas13a can cleave 471 ± 47 copies of reporter every second in the presence of 400 nM reporter (Fig. 1e), or a enzyme catalytic efficiency (k_{cat}/K_M) of 1.2×10^9 M^{-1} s^{-1}, which is 2 orders of magnitude higher than that measured for LbCas12a[11] and consistent with that measured for LbuCas13a based in a bulk assay[12] as well as in a digital assay[13]. This reveals that LbuCas13a is an exceptionally rapid nuclease, operating at the diffusion-limited regime. It is worth noting, however, that the actual enzyme kinetics using di-U reporter (2U) might be slower, as the addition of the poly-U reporter (5U) substantially elevates the local substrate concentration beyond 400 nM, potentially leading to an overestimation of k_{cat}/K_M. This very efficient *trans*-cleavage rate supports its use for rapid, amplification-free detection.

Multiple crRNAs in droplets report the presence of multiple target sequences

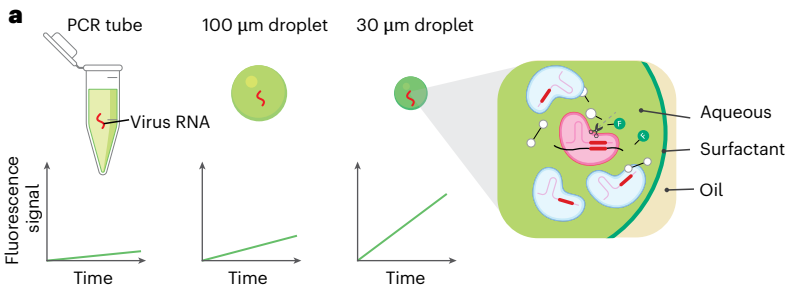
We next tested the effect of crRNA combinations, which can generate more signal per target RNA in bulk[4], in the droplet format. We loaded in vitro-transcribed (IVT) target RNA corresponding to the N gene of SARS-CoV-2 into droplets containing either crRNA 2, crRNA 4, which targets a different region of the N gene, or both crRNAs (Fig. 1f), and then quantified the number and signal of the positive droplets. Surprisingly, while crRNAs 2 and 4 generate similar signals when used individually and might be expected to double the signal when combined[4], we found that the signal per droplet was not significantly different in any of the positive droplets (Fig. 1g). Rather, the number of positive droplets increased when droplets contain both crRNA 2 and crRNA 4 compared with just one of the crRNAs (Fig. 1h). This suggests that RNA corresponding to the IVT N gene was fragmented by Cas13a cleavage upon initiation of the reaction before droplet formation, causing the regions targeted by different crRNAs to be loaded into separate droplets (Fig. 1f). The resulting fragmented loading that we observe is consistent with a study of microwell-based Cas13a reaction[14] and suggests that multiple crRNAs can activate independent single-Cas13a reaction in droplets.

crRNA/target RNA combinations govern Cas13a reaction kinetics

The Cas13a kinetics observed in droplets critically depend on the crRNA and its target. For example, two other crRNAs targeting the SARS-CoV-2 N gene—crRNA 11 and crRNA 12—exhibit significantly slower rates in bulk reactions than crRNA 2 or 4 (Fig. 2a). For this reason, the selection of 'good' crRNAs that maximize Cas13 activity is critical for bulk Cas13-based molecular diagnostics[15], although how different crRNAs affect the activity of Cas13 is not well understood[16]. We therefore tested crRNAs 11 and 12 in our droplet assay and compared their activity with that of crRNA 4. After the droplet reaction was incubated for 15 min, we found that both the number of positive droplets and signal per droplet were reduced for crRNAs 11 and 12 compared with crRNA 4 (Extended Data Fig. 2a,b). By examining the signal time trajectories, we found that the three crRNAs and target sequences resulted in distinct kinetic behaviours, with the slope, shape and *x*-intercept of the individual trajectories varying widely (Fig. 2b–e). In some trajectories, we found a strikingly stochastic behaviour, with periods of no signal increase followed by periods of rapid signal increase ('rugged' versus smooth trajectory). Since each droplet contains, on average, a single target, these results indicate that specific crRNA/target combinations modulate Cas13a enzymatic activity at a single-molecule level.

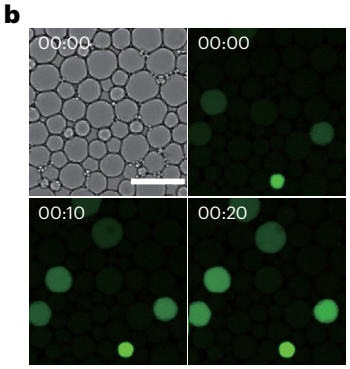
To quantify these kinetic differences, we characterized individual trajectories by their average slope, root-mean-square deviation (RMSD) and time from target addition to initiation of enzyme activity (T_{init}) (Extended Data Fig. 2c). By calculating the instantaneous slopes at each point in the trajectory and fitting their distribution to a Gaussian, we found that the trajectories exhibited two different slopes, one 'fast' when fluorescence was increasing and one 'slow' when fluorescence was not increasing (Extended Data Fig. 2d). Interestingly, even though the average slopes differed significantly for the different crRNAs, the instantaneous 'fast' slopes were constant across all three crRNAs (Extended Data Fig. 3a). Consistent with this, crRNA 12, which exhibited the lowest average slope of the three crRNAs, showed extended 'slow' periods (Extended Data Fig. 3b) and increased level of signal fluctuation (Extended Data Fig. 3c). We found that T_{init} varied significantly among the three crRNAs that we tested, with crRNA 11 exhibiting the slowest T_{init} (Extended Data Fig. 3d), resulting in reduced signal at the reaction endpoint (Extended Data Fig. 2b). To test whether the stochastic behaviour of individual Cas13a reactions is simply caused by the unbinding of crRNAs from the Cas13a protein, we changed the ribonucleoprotein (RNP) concentration to below (for crRNA 4) or above (for crRNA 12) the K_d of the crRNA–Cas13a complex[6,17], but the stochastic behaviour was unaltered (Extended Data Fig. 4a,b). By contrast, when we changed the target from genomic SARS-CoV-2 RNA to a 20-nucleotide fragment complementary to crRNA 12's spacer sequence, the stochastic behaviour of the reaction was no longer observed, and T_{init} was significantly

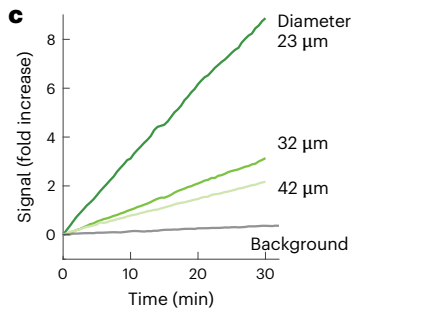
https://doi.org/10.1038/s41551-026-01642-6

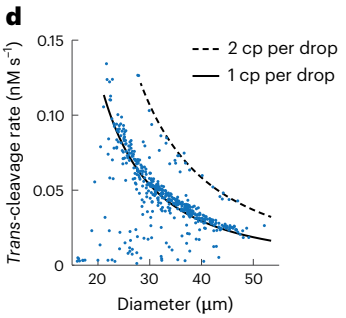


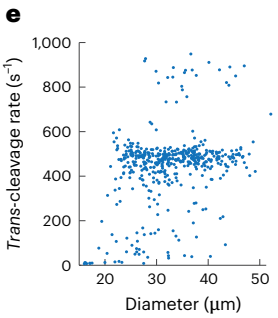
	PCR tube	100 µm droplet	30 µm droplet
Total Cas13	100 nM	100 nM	100 nM
Active Cas13*	1.7×10^{-1} aM	3.3×10^{3} aM	1.2×10^{5} aM
Signal slope	1×	20,000×	714,000×

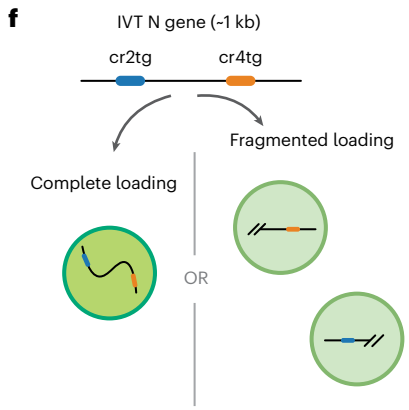
(* Assuming 1 virus copy in the total volume)

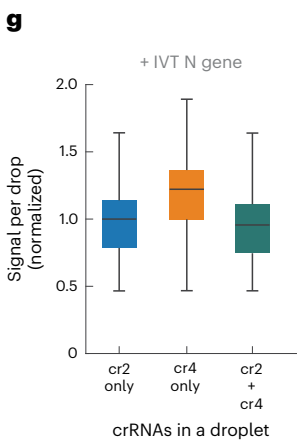












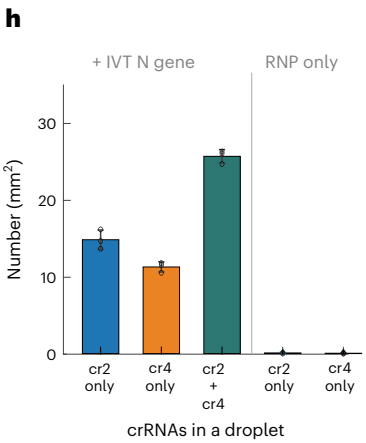


Fig. 1 | A droplet assay measures Cas13a single-molecule kinetics. **a**, Schematic showing the increased signal accumulation rate for a single Cas13a confined in decreasing volumes (red, target RNA). The table quantitatively shows the effect of reaction volume on the signal slope, assuming that only a single target is present. Each droplet contains hundreds of thousands copies of the Cas13a–crRNA ribonucleoprotein (RNP) complexes and millions of quenched RNA reporters. **b**, Bright-field (top left) and fluorescence images of droplet Cas13a reactions taken with a 20× objective lens. $T = 0$ min, 10 min and 20 min since the beginning of imaging. The images shown are representative of three independent experiments, each yielding similar results. Scale bar, 65 µm. **c**, Fluorescence signal over time in three positive droplets (green lines) and one negative droplet (grey line). The signal is calculated from the mean fluorescence intensity change within a droplet normalized by its initial value after background subtraction. An image is taken every 30 s and corrected for photobleaching (Methods). **d**, Single-Cas13a *trans*-cleavage rate measured from individual droplets containing crRNA 4, SARS-CoV-2 RNA and 400 nM 5U-fluorescent reporter ($N = 478$ droplets). **e**, The data in **d** are expressed in turnover frequency by normalizing the signal for droplet size. **f**, Schematic showing two possible outcomes of a Cas13 droplet reaction combining two crRNAs. The RNA targets for crRNA 2 and crRNA 4 are cr2tg and cr4tg, respectively. If the whole N gene is loaded into a droplet containing both crRNAs, the fluorescence signal will accumulate twice as fast as the droplet containing only one target sequence (complete loading). However, if the N gene is fragmented before encapsulation and parts of the N gene are loaded into two different droplets, the number of positive droplets will be doubled, and the signal of each droplet will be the same (fragmented loading). **g**, The results of Cas13a reaction with 2.5×10^{4} copies per µl of IVT N gene and without any target RNA in droplets containing crRNA 2, crRNA 4 or both crRNAs are quantified after 1 h of reaction incubation from three technical replicates. The distribution of signal per droplet is represented as a box and whisker plot showing the median, lower and upper quartiles, and minimum and maximum values ignoring outliers. Data from the triplicate runs were combined for each condition. **h**, Same experiment as described in **f**, but the number of positive droplets is shown. The mean of total positive droplets is 14.8, 11.2, 25.6, 0.08 and 0.04, for crRNA 2, crRNA 4 or both crRNAs with target RNAs and crRNA 2 and crRNA 4 without any target, respectively. The mean and standard deviation were derived from triplicates.

shortened (Extended Data Fig. 4c). This suggests that the kinetic signature of a specific crRNA/target RNA is robust regardless of the variations in the reaction conditions but is sensitive to the crRNA/target RNA sequence and the target RNA length.

Heterogeneous Cas13a kinetics offer a method for multiplexed detection

We hypothesized that the distinct kinetic signatures of the different crRNAs could be used to identify different crRNA–target pairs within a droplet, thus providing a method for multiplexed detection of different RNA viruses (Fig. 2f). To test this idea, which we termed 'kinetic barcoding', we combined a crRNA targeting a common cold virus HCoV-NL-63 (HCoV crRNA 6) and a second crRNA targeting SARS-CoV-2 (crRNA 12). The crRNAs were chosen because they individually exhibit different kinetic signatures on their respective targets (Fig. 2g). We collected 30 min trajectories from hundreds of droplets containing either HCoV-NL-63 or SARS-CoV-2 viral RNA along with Cas13a and both crRNAs together. The two groups of trajectories associated with the two different crRNAs were clearly distinguishable based on their average slope and RMSD (Fig. 2h). On an individual basis, trajectories for HCoV-NL-63 and SARS-CoV-2 were discerned with a 75% accuracy using a support vector machine for binary classification (Methods). To determine how well two viruses can be distinguished when multiple trajectories are combined, we randomly sampled a subset of trajectories and compared their difference by performing Student's *t*-test on their binary classification result (Methods and Fig. 2i). This analysis showed that kinetic barcoding can distinguish between HCoV-NL-63 and SARS-CoV-2 targets within 10 min, provided that 20 or more trajectories (that is, 20 or more positive droplets) are measured (Fig. 2j).

DNA modifications of crRNA can programmably tune Cas13a kinetics

The experiments above with naturally varying enzyme kinetics show the potential of kinetic barcoding for multiplexed detection. However, searching for crRNA/target pairs that exhibit distinct kinetic signatures could be time consuming and is not guaranteed, especially in the case of variants with small numbers of mutations. Building on the observation that regions outside the spacer region affect Cas13a kinetic activity[18], we hypothesized that positioning a single-stranded DNA fragment proximal to Cas13a's HEPN domain will interfere with its *trans*-cleavage activity for RNA without being digested, thus slowing down the rate of reporter RNA cleavage. To test this, we added a DNA fragment of varying length and sequence to the 5′ end of crRNA 4, which was sufficiently long that it could reach the HEPN domain when the crRNA is bound to Cas13a (Fig. 3a). We referred to this hybrid RNA–DNA guide as an 'interfering gRNA', or igRNA. We empirically divided the igRNA into an effector region, which can alter Cas13a's nuclease activity, and an 8-base pair (bp)-long linker region that connects the effector DNA and crRNA. We measured the reporter signal in a solution containing either the igRNA 4 or unmodified crRNA 4 along with synthetic SARS-CoV-2 RNA targets and found that Cas13's *trans*-cleavage rate was reduced for igRNA 4, with DNA effectors having longer lengths and thymines (T) showing stronger reductions (Fig. 3b). The same reduction in signal slope was also observed in single droplets, confirming the change in Cas13 *trans*-cleavage activity at a single-molecule level (Extended Data Fig. 5a). Our result is consistent with the prediction that increasing the local concentration of DNA near the HEPN domain (by adding more nucleotides at the 5′ end of crRNA) or addition of DNA sequences matching the *trans*-cleavage preference (by including thymines in the effector region) will interfere with its nuclease activity more strongly. We concluded that our crRNA modification strategy, which can be used with any target sequences, enables precise tuning of Cas13a kinetics at a single-molecule level.

To investigate the mechanism of this inhibitory behaviour, we conducted atomistic molecular dynamics simulations of the 6T, 8T, 10T, 12T and 12A igRNAs (Methods). We found that for all igRNAs, the 5′ end of the DNA effector moved towards the active site, effectively blocking it (Fig. 3c,d). For all igRNAs, the effector region approached the active site very rapidly. However, we noticed that thymine-based igRNAs converged faster (~25 ns) compared with the 12A igRNA (~100 ns) (Fig. 3d). This observation suggests that there are mostly sequence-agnostic interactions between the linker region and LbuCas13a that bias movement of the DNA effector towards the active site. Furthermore, we noticed that the 8T, 10T and 12T igRNAs all reached distances significantly closer than the 6T and 12A igRNAs supporting previous observations regarding length and sequence constraints needed for effective suppression (Fig. 3b).

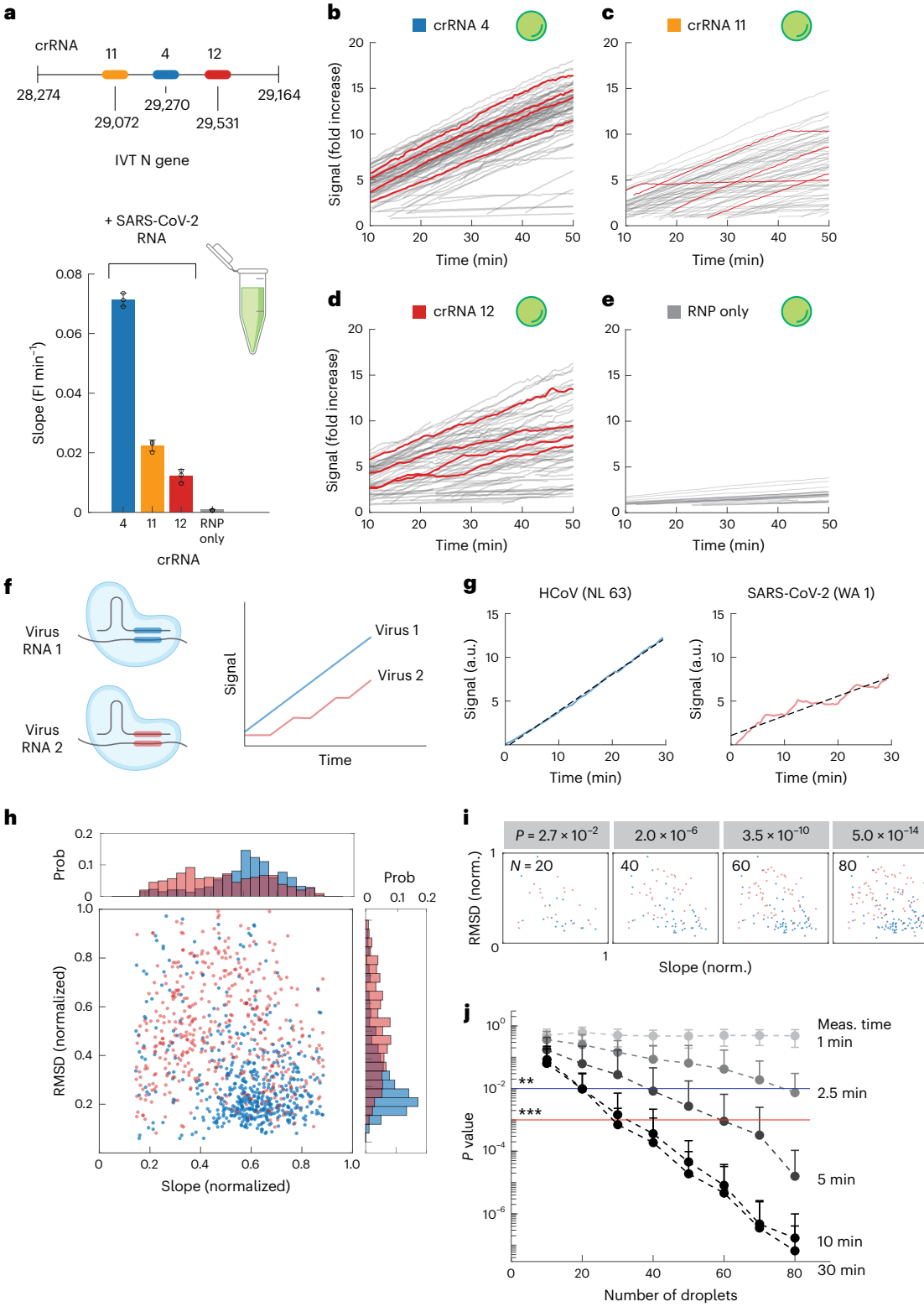
We then sought to determine the residence time for each DNA effector near the active site. We classified the active site as occupied when any nucleotide from the DNA effector was within a 2 nm radius of the active site (see Methods for distance calculations). We found that in agreement with our experimental results (Fig. 3b), active site occupancy increased proportionally with DNA effector length for thymine-based igRNAs (Fig. 3e). The 8T, 10T and 12T igRNAs showed more consistent active site occupancy than the 6T igRNA or 12A igRNA (Fig. 3e), suggesting that sequence selectivity occurs in the surface region near the active site (Supplementary Videos 2, 3 and 4). Although we noticed similar occupancies between the 8T, 10T and 12T igRNAs, we reason that at longer timescales, the larger amount of thymines able to reach the active site for the 12T igRNA explains the higher suppression for this igRNA compared with the 8T and 10T. We speculate

Fig. 2 | Cas13a kinetics are dependent on the crRNA and target RNA. a, The results of a bulk Cas13a reaction (fluorescence slope) with 3.5×10^4 copies per µl of SARS-CoV-2 RNA for crRNAs targeting different regions of the SARS-CoV-2 N gene. The RNP-only condition is measured with all three crRNAs. The slope is determined by performing simple linear regression of data from each replicate ($N = 3$) individually. Data are represented as mean ± s.d. **b**, Time trajectories of single-Cas13a reactions using crRNA 4. One hundred individual trajectories are measured in droplets ranging from 30 µm to 36 µm in diameter (grey lines), and representative trajectories are highlighted (red lines). The signal is measured every 30 s and represented as fold increase from the initial value. Two replicate experiments were combined for each crRNA. **c**, The same experiment as described in **b**, but with crRNA 11. **d**, The same experiment as described in **b**, but with crRNA 12. **e**, Time trajectories of droplets containing no target RNA but generating a non-zero signal from a Cas13a reaction. Thirty-one individual trajectories from two replicate runs were measured in droplets ranging from 30 µm to 36 µm in diameter. **f**, Schematic showing the principle of kinetic barcoding for detection of two different viruses in the same droplet reaction. It relies on the unique Cas13a kinetic signatures for specific combinations of a crRNA and target. **g**, Representative single-Cas13a reaction trajectories with HCoV-NL-63 RNA (targeted by crRNA 7) or SARS-CoV-2 RNA (targeted by crRNA 12). The signal is the total fluorescence change in a droplet normalized by its initial value, which remains invariant regardless of droplet size. The dotted black line shows a linear fit. **h**, Distribution of slope and RMSD of individual Cas13a trajectories between HCoV-NL-63 and SARS-CoV-2 RNA. The slope and RMSD are determined from individual 30-min-long trajectories ($N = 551$ for HCoV-NL-63 and $N = 488$ for SARS-CoV-2) measured with a single crRNA–target pair. The normalized RMSD is rescaled from 0 to the highest value of the dataset. The slope is rescaled from 0 to the highest value in the dataset (blue, HCoV-NL-63; red, SARS-CoV-2). **i**, Identification of HCoV-NL-63 or SARS-CoV-2 based on the kinetic parameters of individual Cas13a reactions. Varying numbers of 30-min-long Cas13a trajectories are randomly selected from each condition, and the difference between two groups are quantified as *P* values based on a two-tailed Student's *t*-test. **j**, The accuracy of kinetic barcoding quantified as *P* values based on a two-tailed Student's *t*-test. *P* values are determined for decreasing measurement times by taking the initial parts of Cas13a trajectories. Data show mean ± s.d. of 50 repeated iterations. ** (blue line) $P < 0.005$, *** (red line) $P < 0.001$. FI, fluorescence; Prob, probability; norm., normalized; Meas., measuring.

https://doi.org/10.1038/s41551-026-01642-6

that the mechanism for this sequence preference reflects LbuCas13a's previously characterized nucleotide cleavage preferences[18].

We next tested whether our programmable kinetic barcoding strategy can improve multiplexed virus detection. We first selected 4 different crRNAs targeting different virus RNA that all provided identical *trans*-cleavage rates for their respective target (crRNA 4 for SARS-CoV-2 wild-type, crRNA delta for SARS-CoV-2 delta, crRNA NL63 for HCoV-NL-63 and crRNA H3N2 for H3N2 influenza virus), and hence could not be used to distinguish viral targets based on kinetics in a droplet Cas13 assay (Extended Data Fig. 5b). We then added effector DNA of increasing lengths to each crRNA and measured 1 h trajectories from droplets containing individual target virus RNA. We observed that the trajectories were linear, and their slopes were clearly separated from one virus to another (Fig. 4a and Extended Data Fig. 5c). Importantly, the slopes for each individual virus remained the same even when all four crRNAs were combined into the same droplet (Extended Data Fig. 5d,e), making it possible to simultaneously detect different targets based on their unique slopes. One exception was



https://doi.org/10.1038/s41551-026-01642-6

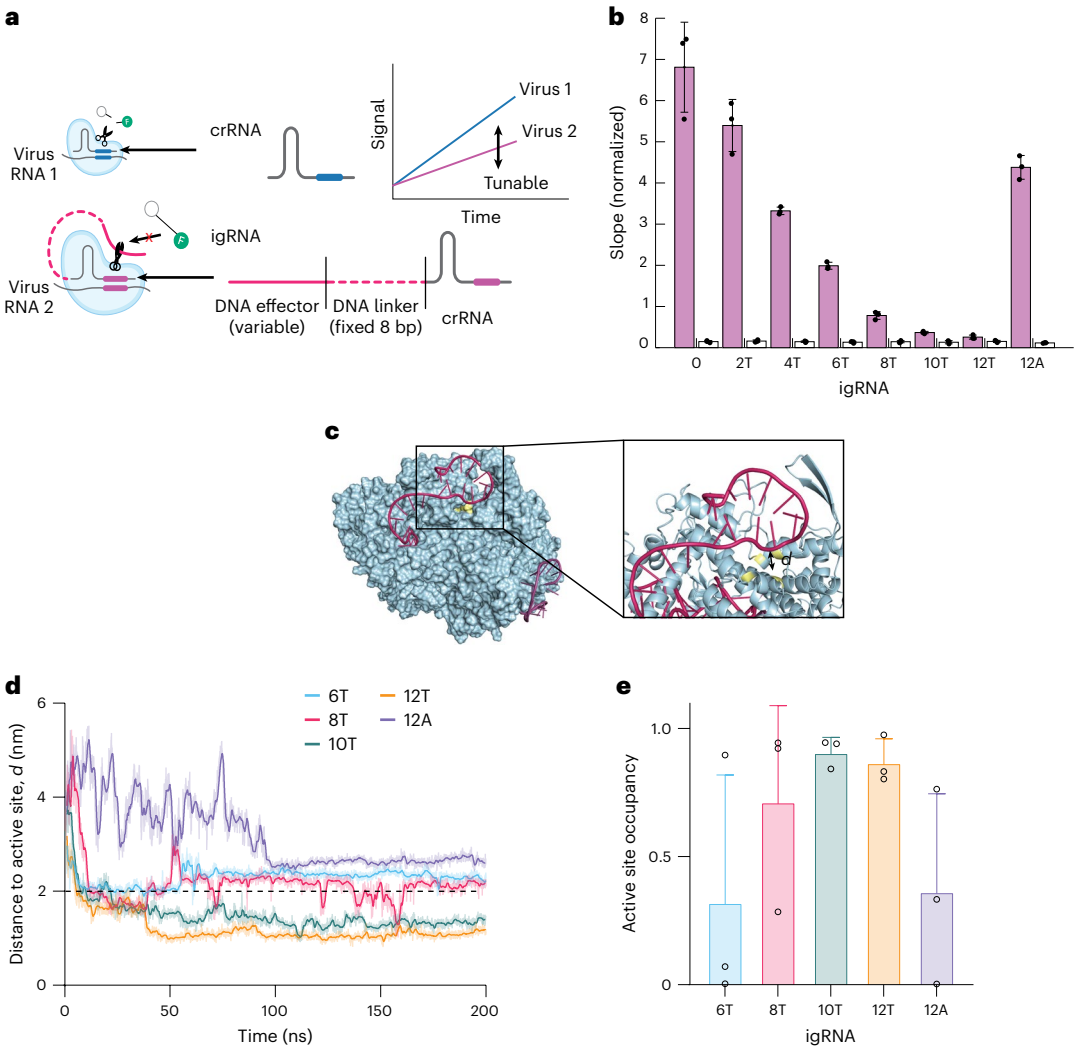


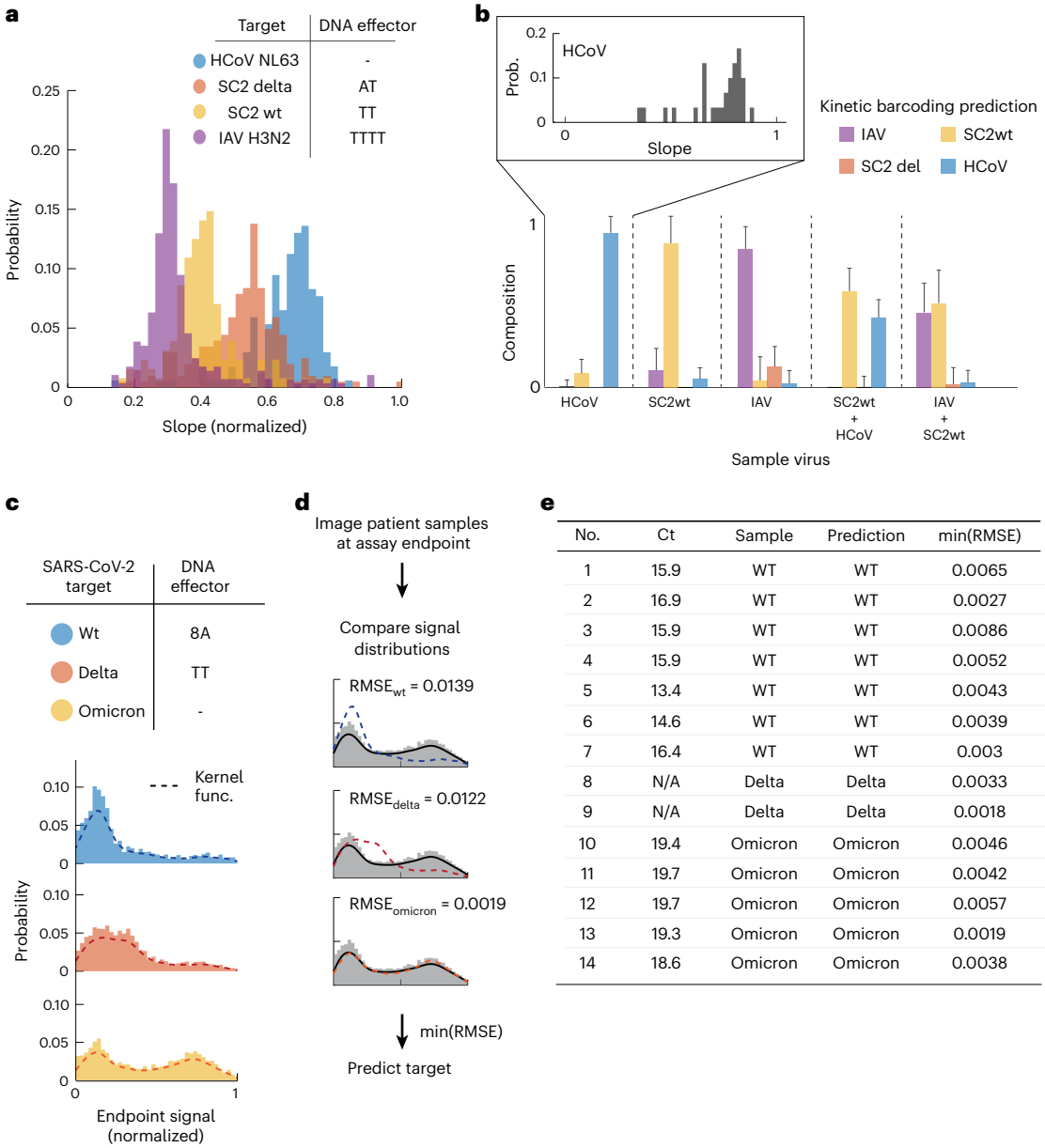
Fig. 3 | Kinetic barcoding for multiplexed detection of viruses and variants. **a**, Schematic showing the principle of kinetic barcoding with igRNA. DNA effector of varying sequence and length is added in the 5′ end of crRNA through a fixed, 8-bp-long DNA linker, leading to interference with the HEPN nuclease activity. **b**, Bulk Cas13 reaction rate is altered by igRNA. DNA effector with varying numbers of Ts or 12A is added to crRNA 4, and the reaction rate is measured with a fixed amount of synthetic target RNA (filled bar) or RNP only (hollow bar). Slopes were normalized to the mean slope of each replicate batch to account for batch-to-batch variability. Data are represented as mean ± s.d. of three replicates. **c**, DNA effector blocks LbuCas13a active site. Representative snapshot at $t = 200$ ns of molecular dynamics simulation for 12T igRNA. The igRNA (red) residues position themselves directly on top of the LbuCas13a (light blue) active site (yellow). Inset: d represents the shortest distance from DNA effector of igRNA to the centre of mass for the catalytic site (R472, H477, R1048 and H1053). **d**, Dynamics of active site occupancy by DNA effector represented as d over time. Solid lines represent moving average over 1 ns simulation time, and translucent lines represent raw data. **e**, Occupancy of active site changes based on DNA effector length and sequence. Active site occupancy as a fraction of total simulation time (200 ns) for each igRNA. Data are represented as mean ± s.d. of three replicates.

SARS-CoV-2 delta, which showed two peaks when the crRNAs were combined since both crRNA 4 and crRNA delta targeted its RNA. We focused on the three viruses exhibiting a single peak with the crRNA combination and classified samples containing either one or two different viruses based on their slopes (Methods). We found that our programmable kinetic barcoding approach not only correctly identified the target but also quantified the proportion of each target among the possible single or dual infection scenarios (Fig. 4b and Extended Data Fig. 6).

Endpoint kinetic barcoding can accurately differentiate virus variants

From a practical perspective, evaluating a multiplexed RNA detection assay with a single measurement would be much preferred over the requirement to collect a series of measurements over time. To that end, we explored whether kinetic barcoding was a viable strategy if only the endpoint fluorescence of droplets was measured rather than their full-time trajectory, a realistic possibility since the programmable kinetic barcoding strategy alters only reaction slope without introducing additional stochasticity. We first built a rapid imaging platform that consisted of a low magnification objective (2.5×/numerical aperture (NA) 0.085) and an automated stage that could image the approximately 160,000 droplets from a single 20 µl reaction in 45 s (Methods). We then tested whether endpoint kinetic barcoding could be used with patient samples to differentiate two dominant SARS-CoV-2 variants circulating between November 2020 and January 2022—delta and omicron—from wild-type SARS-CoV-2. In addition to crRNA 4 targeting a conserved region of SARS-CoV-2 RNA, we chose two crRNAs that are specific to unique mutations in delta (crRNA delta) or omicron (crRNA omicron) and added effector DNA modifications to differentiate their kinetics (Fig. 4c). We tested different virus targets with the 3-crRNA combination and imaged the droplets after 1 h incubation

https://doi.org/10.1038/s41551-026-01642-6



e

No.	Ct	Sample	Prediction	min(RMSE)
1	15.9	WT	WT	0.0065
2	16.9	WT	WT	0.0027
3	15.9	WT	WT	0.0086
4	15.9	WT	WT	0.0052
5	13.4	WT	WT	0.0043
6	14.6	WT	WT	0.0039
7	16.4	WT	WT	0.003
8	N/A	Delta	Delta	0.0033
9	N/A	Delta	Delta	0.0018
10	19.4	Omicron	Omicron	0.0046
11	19.7	Omicron	Omicron	0.0042
12	19.7	Omicron	Omicron	0.0057
13	19.3	Omicron	Omicron	0.0019
14	18.6	Omicron	Omicron	0.0038

Fig. 4 | Endpoint kinetic barcoding with clinical samples. a, Measurement of four different viruses with modified crRNAs containing different DNA effectors (top). Total *N* from two replicate measurements were 169, 406, 128 and 285 for HCoV NL63, SARS-CoV-2 (SC2) delta, SC2 wt and IAV H3N2. Signal slope is normalized for droplet size, and its distribution is shown in histogram. **b**, Prediction of target viruses based on the signal slope distribution. From more than 100 trajectories obtained for each sample in 2 replicate experiments, 30 trajectories are randomly selected to mimic samples with intermediate virus concentrations (representative distribution shown in the inset and in Extended data Fig. 6) and the virus compositions in the sample are predicted. The bar graph shows the mean and standard distribution of target predictions from 100 repeated sampling. **c**, Design of crRNAs for multiplexed SC2 variant detection (top). Droplet Cas13a reaction is incubated with an individual variant's synthetic RNA to obtain the standard curve (bottom). The dotted line indicates the kernel function of slope distribution. **d**, Clinical sample analysis scheme. The kernel function of clinical samples is compared with the standard curves obtained in **a**. The one that provides the smallest difference, measured in terms of RMSE between two curves, is selected as the target. **e**, Summary of clinical samples and kinetic barcoding prediction result. The Ct values are obtained from the N gene. For SC2 delta virus, RNA isolated from a cell was used (BEI resources) instead of the patient sample. func., function; N/A, not available.

using the endpoint detection system. As expected, the wild-type virus RNA showed a single peak distribution, while the delta or omicron RNA exhibited two peaks—one corresponding to the variant and the other to the shared region of SARS-CoV-2 genome (Fig. 4c). To classify each clinical sample, we compared its signal distribution with the three reference curves that we collected and identified the one that exhibited the least difference as determined by root mean square error (RMSE) or the Kolmogorov–Smirnov test (Fig. 4d and Extended Data Fig. 7a). Focusing on samples with mid-to-high virus concentrations (Ct < 20), we tested 15 positive SARS-CoV-2 samples and accurately classified all samples through kinetic barcoding (Fig. 4e and Extended Data Fig. 7b).

Discussion

In summary, we demonstrate that a droplet-based Cas13a direct detection assay can distinguish RNA targets based on single-Cas13 reaction kinetics. We found that LbuCas13a is an efficient, diffusion-limited enzyme, whose kinetics are controlled by the specific combination of the crRNA and the target[19,20]. Interestingly, the distribution of Cas13a

RNP trajectories is largely homogeneous for crRNAs supporting high enzymatic activities (Fig. 2b), implying that the active conformation of Cas13a RNP is stable over time. However, certain crRNAs were found to induce stochastic trajectories on the timescale of minutes. The observation that this kinetic feature is abolished when a short RNA target is used instead of the longer viral RNA (Extended Data Fig. 4c) suggests a role of local or global RNA structure on modifications in the kinetics of an individual Cas13a.

We first took advantage of these characteristic kinetic signatures to show that different viral targets could be distinguished in a single droplet. We then devised a simple crRNA modification strategy that enables programmable tuning of LbuCas13's *trans*-cleavage rate, expanding the diagnostic utility of kinetic barcoding and the number of targets that could be distinguished simultaneously. Kinetic barcoding relies on reading the crRNA/target RNA-dependent single-Cas13a activity, which was possible because the early fragmentation of a target RNA before droplet formation generated multiple droplets containing a single, distinct target fragment (Fig. 1f). We demonstrate this principle by multiplexing four targets, but we anticipate that kinetic barcoding of more can be achieved with further development of the assay and LbuCas13a itself, as well as by combining natural and programmed kinetic barcoding.

The kinetic barcoding strategy that we present represents a new approach to multiplexing based on single-enzyme kinetics, adding a new dimension to RNA detection that could enhance existing multiplexing strategies. Previous CRISPR–Cas-based assays achieved multiplexed detection by using multiple Cas orthologues acting on different colour reporters[7] or massively dividing reactions after amplification into droplets that each detect only a single target[21]. Kinetic barcoding could be readily combined with colour-based methods to immediately achieve multiplexing of more than ten target pathogens or with the multiplexed droplets to act as a multiplier. A deeper understanding of the kinetics and mechanisms of Cas13 and other CRISPR nucleases will also offer new opportunities in diagnostic and therapeutic development.

While kinetic barcoding offers a powerful dimension for multiplexing, the stochastic nature of single-molecule reaction initiation remains a practical limitation; if not carefully balanced, these timing variations can introduce noise that endpoint measurements may not fully capture. Future engineering of 'synchronized' CRISPR systems—utilizing, for example, light-triggerable Cas13 system[22] or other inducible activation methods—could align reaction start times to further enhance diagnostic precision. Our kinetic barcoding strategy remains compatible with existing commercial digital assay hardware by integrating kinetics analysis software, although the larger compartment volumes typical of these platforms may require further assay optimization to compensate for signal attenuation. For broader clinical and point-of-care applications, we envision the adaptation of kinetic barcoding to bulk formats. If kinetic features can be normalized against varying target concentrations, this would enable high-order multiplexing while bypassing the requirement for complex microfluidic compartmentalization.

Methods

Protein purification

Protein purification was performed as previously described[4]. In brief, the LbuCas13a expression vector contains the codon-optimized Cas13a genomic sequence, N-terminal His6-MBP-TEV cleavage site sequence and a T7 promoter binding sequence (Addgene plasmid number 83482). The protein is expressed in Rosetta 2 (DE3) pLysS *E. coli* cells in Terrific broth at 16 °C overnight. Soluble His6-MBP-TEV-Cas13a was isolated over metal ion affinity chromatography, and the His6-MBP tag was cleaved with TEV protease at 4 °C overnight. Cleaved Cas13a was loaded onto a HiTrap SP column (GE Healthcare) and eluted over a linear KCl (0.25–1.0 M) gradient. Cas13a-containing fractions were further purified via size-exclusion chromatography on an S200 column (GE Healthcare) in gel filtration buffer (20 mM HEPES-K pH 7.0, 200 mM KCl, 10% glycerol, 1 mM TCEP) and were subsequently flash frozen for storage at −80 °C.

Preparation of SARS-CoV-2 RNA segments

In vitro RNA transcription is performed as previously described[4]. SARS-CoV-2 N gene, S gene (wild type (WT)) and S gene with D614G mutation were transcribed off a single-stranded DNA oligonucleotide template (IDT) using the HiScribe T7 Quick High Yield RNA Synthesis Kit (NEB) following the manufacturer's recommendations. Template DNA was removed by addition of DNase I (NEB), and IVT RNA was subsequently purified using RNA STAT-60 (AMSBIO) and the Direct-Zol RNA MiniPrep Kit (Zymo Research). RNA concentration was quantified by Nanodrop, and copy number was calculated using transcript length and concentration.

Preparation of full viral genomic RNA

Full viral genomic RNAs are purified as previously described[4]. Isolate USA-WA1/2020 of SARS-CoV-2 (NR-52281 BEI Resources) and CA427 (B.1.427, received from CA DPH) were propagated in Vero CCL-81 cells (ATCC). Isolate Amsterdam I of HCoV-NL-63 (NR-470, BEI Resources) was propagated in Huh7.5.1-ACE2 cells (gift from A. Puschnik), which were previously generated in Wang et al. 2021[23] (all virus cultures were performed in a Biosafety Level 3 laboratory). RNA was extracted from the viral supernatant via RNA STAT-60 (AMSBIO) and the Direct-Zol RNA MiniPrep Kit (Zymo Research).

SARS-CoV-2 patient samples

Patient samples were obtained from a UC Berkeley campus testing programme, as previously described[24]. In brief, human mid-turbinate nasal/oropharyngeal swabs were collected, processed and tested by running quantitative reverse transcription polymerase chain reaction (qRT-PCR) on extracted RNA using primers for SARS-CoV-2. Ct values were obtained using primers for the N gene, S gene and Orf1ab of the SARS-CoV-2. Sequence data for each sample were used to identify SARS-CoV-2 variants. The samples used in this study were non-identifiable biospecimens, for which there was no link to identifiable subject information. Only secondary data analysis was carried out on the samples, and the research data will not be held for inspection by nor submitted to the US Food and Drug Administration (FDA).

crRNA design

All unmodified crRNAs targeting SARS-CoV-2, SARS-CoV-2 variants delta (SΔ157–158) and omicron (NΔ31–33), HCoV-NL-63 or influenza H3N2 were ordered as desalted oligonucleotides from Synthego at a scale of 5 nmole (Supplementary Table 1). Select crRNAs have also been previously described[4,5]. All DNA-modified crRNAs are ordered from Integrated DNA Technologies at a scale of 4 nmole (Supplementary Table 1).

Bulk Cas13a nuclease assays

LbuCas13a–crRNA RNP complexes were first preassembled at 133 nM equimolar concentration for 15 min at room temperature and then diluted to 25 nM LbuCas13a in cleavage buffer (20 mM HEPES-Na pH 6.8, 50 mM KCl, 5 mM $MgCl_2$ and 5% glycerol) in the presence of 400 nM of reporter RNA (5′-Alexa488rUrUrUrU-IowaBlack FQ-3′), 1 U μl^{-1} Murine RNase Inhibitor (NEB, catalogue number M0314), 0.1 vol% IGEPAL 630 (Fisher, catalogue number ICN19859650) and varying amounts of target RNA. For reactions using more than one crRNA, multiple crRNAs were combined at an equal concentration and subsequently the total crRNA mix was assembled with Cas13a at a 133 nM equimolar concentration. The RNP complex (25 nM) is used unless specified otherwise. The reaction mix is measured either in bulk or in droplet following emulsification ('Droplet formation'). For the bulk Cas13a assay, the reactions were loaded into a 384-well (Corning, catalogue number 3820) incubated in a fluorescence plate reader

(TECAN, Infinite 200Pro) for 60 min at 37 °C with fluorescence measurements taken every 2.5 min (λ_{ex}, 485 nM; λ_{em}, 535 nM; gain, 130). Background-corrected fluorescence values were obtained by subtracting fluorescence values obtained from reactions carried out containing only reporter and buffer. The slope of Cas13a reaction is calculated by simple linear regression of raw data from time 0 for the set duration.

Droplet formation

To emulsify the Cas13a reaction mix, 20 µl of the aqueous mix was combined with 100 µl of HFE-7500 oil supplemented with 2% (w/w) PEG–PFPE amphiphilic block copolymer surfactant (008-Fluoro-surfactant, RAN Biotechnologies) in a 0.2 ml 8-tube strip. The oil/aqueous mix was emulsified by repeated, fully automated pipetting using an electronic 8-channel pipette (Integra-biosciences, part number 4623) fitted with a 300 µl pipet tip (Integra-biosciences, part number 3835). A sample volume of 110 µl was mixed for 150 repetitions at the maximum speed (speed 10) to generate droplets of a narrow size range. The emulsion was either directly loaded into a flow cell for the time course imaging or incubated in a heating block at 37 °C before being transferred and imaged. In cases where imaging could not be performed immediately after the reaction, the emulsion was quenched on ice until imaging. For the time course imaging experiment, the emulsion was quickly separated by spinning in a speed-controlled mini-centrifuge (~100 × *g*) for 10 s, the oil was completely removed from the bottom of the tube, and the emulsion was transferred into a custom imaging chamber after several cycles of gentle manual mixing. It took approximately 10 min from droplet formation to the start of image acquisition.

A custom imaging chamber for droplet imaging

The sample flow cell was prepared by sandwiching double-sided tape (~20 µm thick, 3M catalogue number 9457) between an acrylic slide (75 mm × 25 mm × 2 mm, laser cut from a 2-mm-thick acrylic plate) and a siliconized coverslip (22 mm × 22 mm × 0.22 mm, Hampton Research catalogue number 500829). Both surfaces are hydrophobic, promoting thin layers of oil between droplets and the surface. Siliconized coverslips were rinsed with isopropanol to remove any auto-fluorescent debris (20 min sonication) and spin-dried before assembly. Sample emulsion (15 µl) is loaded into the flow cell by capillary action, after which the inlet and outlet are sealed with Valap (1:1:1 Vaseline/lanolin/paraffin).

For an increased throughput of samples using the pipetting robot, a custom imaging chamber was built containing eight independent flow cells. Each flow cell (39 mm × 6.6 mm × 0.026 mm) consisted of a double-sided adhesive (ARcare 8026, Adhesives Research) bonded between an acrylic slide (75 mm × 50 mm × 1.5 mm, laser cut from a 1.5-mm-thick acrylic plate) and a large glass microscope slide (75 mm × 51 mm × 1.2 mm). Before the assembly, the large glass microscope slides were sonicated in 2% liquid detergent (Neutrad, Decon labs) for 30 min at 55 °C followed by a rinsing step with MilliQ water and blow dry using a compressed air blow gun. After the assembly, the imaging chamber was placed on an acrylic chamber holder where the pipetting robot loaded the sample emulsion on the inlet ports of each well simultaneously using an automated program. Once the droplets filled the total volume of the independent flow cells, the imaging chamber was ready to be imaged.

Microscopy and data acquisition

Droplet imaging was carried out for both high-resolution (low-throughput) and low-resolution (high-throughput) studies. The high-resolution imaging was carried out on an inverted Nikon Eclipse Ti microscope (Nikon Instruments) equipped with a Yokogawa CSU-X spinning disk. A 488 nm solid-state laser (ILE-400 multimode fibre with BCU, Andor Technologies) was used to excite the RNA probe, and the fluorescence light was spectrally filtered with a 535/40 nm emission filter (Chroma Technology) and imaged on an sCMOS camera (Zyla 4.2, Andor Technologies). A 20× water-immersion objective (CFI Apo LWD Lambda S, NA 0.95) was used with the Perfect Focus System to monitor droplets during the reaction or to accurately quantify fluorescence signal at reaction endpoint. Fluorescent reporter (400 nM) was added to the reaction. Images were acquired through Micro-Manager with 500 ms exposure time and 2 × 2 camera binning. Typically, 16 fields of view (FOVs) were acquired every 30 s for the time course imaging, and 36 FOVs are acquired for the endpoint imaging. The low-resolution imaging was carried out on a Zeiss Axiovert with a 2.5× objective (Plan-NEOFLUAR, NA 0.085) to capture droplet reaction endpoints after 30 min or 1 h of reaction time. A xenon light source with a 470/40 nm excitation filter (Chroma Technology) and a 535/40 nm emission filter (Chroma Technology) was used. Fluorescent reporter (1.6 µM) was added to the reaction, which increased both the signal and background compared with the reaction containing 400 nM reporter. To image all the droplets for 8 independent reactions simultaneously on the custom imaging chamber, 7 FOVs were acquired per reaction with 6 s exposure time without camera binning.

Droplet detection

We used MATLAB (MathWorks R2020b) to detect positive droplets and quantify fluorescence signals from microscopy images. First, the greyscale images were converted to binary images based on a locally adaptive threshold. The threshold is defined generously to select all the positive droplets and potentially some negative droplets or debris at this stage. Second, connected droplets were separated by watershed transform. Third, individual droplets are identified by looking for circular continuous regions and droplet parameters such as radius, circularity and fluorescence signal are quantified. Fluorescence signal is quantified in two different ways: the mean fluorescence signal of a droplet reflecting the density of cleaved reporter; the total fluorescence signal reflecting the total amount of cleaved reporter within a droplet. Lastly, positive droplets are chosen based on their circularity and total fluorescence signal by applying a threshold that was consistently used throughout the experiments.

Droplet tracking in time course images

To quantify signal accumulation in the same droplet over time, we associated droplets over time based on their motion estimated by a Kalman filter in MATLAB. The filter is used to predict the track's location in each frame and determine the likelihood of each detection being assigned to each track. Only the droplets showing continuous trajectories in time and magnitude are selected for the downstream analysis.

Comparison of single-Cas13a reaction with enzyme kinetics

We analysed the Cas13a reaction with a single crRNA (Fig. 1e) using the Michaelis–Menten enzyme kinetics model with the quasi-steady-state approximation:

$$v = \frac{k_{cat}[E_0][S]}{K_M + [S]},$$

where v is the reaction rate, $[E_0]$ is the ternary Cas13a, $[S]$ is the free RNA reporter, and k_{cat} and K_M are the catalytic rate constant and the Michaelis constant, respectively. We assumed low substrate concentration ($[S] \ll K_M$) since the RNA reporter $[S]$ is 400 nM and K_M is estimated to be larger than 1 µM (ref. 25) and simplified the equation to

$$v = \frac{k_{cat}[E_0][S]}{K_M}$$

$v/[E_0]$ is turnover frequency, or the reciprocal of the mean waiting time $\langle 1/t \rangle$ in the single-molecule Michaelis–Menten framework[26], and it can be obtained from Fig. 1d,e after converting the fluorescence signal to molar concentration of cleaved reporter based on a calibration.

Analysis of Cas13a time trajectories

We processed the raw signal in a series of steps before analysis. First, we corrected for the global signal fluctuation, which arise from a slight drift in *z*-focus even with the Perfect Focus System; we characterized the global signal from the background droplets as the mean of their pixel values and divided it from the positive droplet signal in each image frame. Second, we corrected for the photobleaching; we first characterized the signal decay rate from >200 Cas13a curves exhibiting negative slopes and positive initial signals. We modelled photobleaching as a linear function of the initial signal based on the observed linear relationship between the decay rate versus initial signal ($R^2 = 0.87$). Using the model, we corrected for photobleaching in each trajectory point by point. Third, we filtered the trajectories with a weak Savitzky–Golay filter (order 5, frame length 9) to remove the high-frequency measurement noise while preserving overall structure of the curve. Lastly, we calculated instantaneous slopes by dividing signal change between frames by the frame interval and removed single outliers exhibiting high positive or negative slopes. To characterize key parameters of Cas13a kinetics, we analysed individual trajectories in two different domains. First, we determined the slope, T_{init} and RMSD from signal time trajectories by linear regression. Since T_{init} indicates time since the droplet reaction was started, we added a constant time (12.5 min) that took from Cas13 droplet formation until the beginning of time course imaging. Second, we determined the $slope_{fast}$, $slope_{slow}$ and a fraction spent in each period by fitting a Gaussian probability density function (pdf) to the instantaneous slope distribution. We compared the model qualities between the single versus binary Gaussian pdfs using Akaike's information criterion to determine whether a trajectory exhibits two different periods of slope or not.

Kinetic barcoding with unmodified crRNAs

We used the slope and RMSD of individual signal trajectories to compare Cas13a reactions between different target crRNAs. We first performed binary classification of trajectories based on support vector machine in MATLAB. For this, we collected 200–400 signal trajectories in each condition, in 2 or more independent experiments per condition to prevent bias. We converted the trajectories into a two-dimensional array consisting of the slope and RMSD and divided the array into a training and a validation set. We then trained an algorithm using the training set with the known answers (that is, target-crRNA condition) and classified the validation set. The accuracy of identifying individual trajectories was 75% for HCoV-NL-63 versus SARS-CoV-2. To assess the difference between two groups of trajectories, we evaluated *P* values for the predicted classes using a two-tailed Student's *t*-test.

Kinetic barcoding with signal slope of IgRNAs

The goal of this analysis was to quantify virus compositions of a sample from its slope distribution, assuming that any permutations of single or multiple co-infections could be present. The slopes obtained from either unmodified crRNA or IgRNAs exhibited distributions with partial overlap between each other. To statistically predict the class of a measured slope, we used a multiclass error-correcting output codes model using support vector machine binary learners. We trained a model based on the slope distribution of four different classes (that is, crRNA and igRNAs). From the model, we obtained class posterior probabilities, which assigns relative probabilities that a given slope could be measured from one class versus the others. To quantify the virus composition of an unknown sample, we converted the slope distribution to the matrix of class posterior probabilities. We then quantified virus compositions by summing the posterior probability of individual classes.

Kinetic barcoding with endpoint signal of IgRNAs

The goal of this analysis was to classify the variant information of a sample from three possible cases (that is, SC2 wild-type, SC2 delta and SC2 omicron). For this, we characterized the kernel function of individual SARS-CoV-2 variants by measuring fluorescence signal with virus RNA isolated from a cell. For a patient sample, we compared its kernel function with the three reference functions and quantified their difference in terms of RMSE. We chose the variant with the lowest RMSE value. As an alternative to using the kernel function, we also used the Kolmogorov–Smirnov test, which compares two cumulative distribution functions without any filters and obtained consistent result.

Molecular dynamics simulations

Simulations were based on the structure of *Leptotrichia buccalis* (Lbu) Cas13a in complex with a crRNA and target RNA (PDB 5XWP), obtained by single-wavelength anomalous diffraction at 3.08 Å resolution[27]. The complete structure with inclusion of missing atoms and reinstated catalytic residues R1048 and H1053, which were mutated for alanine in the crystal structure, were obtained from the SWISS-MODEL homology modelling repository[28,29]. PyMOL was used to mutate RNA sequences and build nucleotides for the inhibitory segment. All histidine residues were treated as singly protonated in the ε position based on previous literature on Cas13a simulations[30].

All molecular dynamics simulations were conducted using GROMACS (version 2024.1)[31] and the AMBER ff14SB force field[32], including the χOL3 corrections for RNA[33,34] and OL15 corrections for DNA[35–37]. We used the TIP3P model for water molecules[38].

Systems were solvated on a dodecahedron box with 50 mM KCl and 5 mM $MgCl_2$ and neutralized by addition of Na^+ counterions to simulate reaction conditions. First, all systems were subjected to a 50,000-step energy minimization using the steepest descent algorithm to prevent any steric clashes. Then, the systems were heated in two consecutive isochoric (NVT) ensembles, to 300 K for 100 ps and then to 310 K for 100 ps. Temperature was kept constant using velocity rescaling with a 0.1 ps time constant. Afterwards, the system's density was equilibrated in the isobaric ensemble (NPT) for 100 ps by coupling the pressure to 1 atm using a C-rescale barostat with a time constant of 2 ps. All bond lengths of hydrogen atoms were constrained using the SHAKE algorithm. Long-range electrostatic calculations were conducted using the particle-mesh-Ewald algorithm. Electrostatic and van der Waals cut-off values were both set to 1.2 nm. Finally, all position constraints were released, and production runs of 200 ns were carried out in the NVT ensemble using a 2 fs integration step.

Distances for Fig. 3d,e were computed by measuring the shortest distance from any atom of the DNA effector region to the centre of mass for the catalytic site (R472, H477, R1048 and H1053) across the entire simulation time.

Reporting summary

Further information on research design is available in the Nature Portfolio Reporting Summary linked to this article.

Data availability

All data that support the findings of this study are provided in the Source Data files. Source data are provided with this paper.

References

1. CDC. Similarities and differences between flu and COVID-19. *Centers for Disease Control and Prevention* https://www.cdc.gov/flu/symptoms/flu-vs-covid19.htm (2022).
2. The BioFire® FilmArray® System. *BioFire Diagnostics* https://www.biofiredx.com/products/filmarray/ (2024).
3. Cepheid | Multi. https://www.cepheid.com/en/systems/Multiplexing (2026).
4. Fozouni, P. et al. Amplification-free detection of SARS-CoV-2 with CRISPR-Cas13a and mobile phone microscopy. *Cell* **184**, 323–333. e9 (2021).

5. Liu, T. Y. et al. Accelerated RNA detection using tandem CRISPR nucleases. *Nat. Chem. Biol.* **17**, 982–988 (2021).
6. East-Seletsky, A. et al. Two distinct RNase activities of CRISPR-C2c2 enable guide-RNA processing and RNA detection. *Nature* **538**, 270–273 (2016).
7. Gootenberg, J. S. et al. Multiplexed and portable nucleic acid detection platform with Cas13, Cas12a, and Csm6. *Science* **360**, 439–444 (2018).
8. Gootenberg, J. S. et al. Nucleic acid detection with CRISPR-Cas13a/C2c2. *Science* **356**, 438–442 (2017).
9. Byrnes, S. A. et al. Simple polydisperse droplet emulsion polymerase chain reaction with statistical volumetric correction compared with microfluidic droplet digital polymerase chain reaction. *Anal. Chem.* **90**, 9374–9380 (2018).
10. Ramachandran, A. & Santiago, J. G. CRISPR enzyme kinetics for molecular diagnostics. *Anal. Chem.* **93**, 7456–7464 (2021).
11. Chen, J. S. et al. CRISPR-Cas12a target binding unleashes indiscriminate single-stranded DNase activity. *Science* **360**, 436–439 (2018).
12. Shan, Y., Zhou, X., Huang, R. & Xing, D. High-fidelity and rapid quantification of miRNA combining crRNA programmability and CRISPR/Cas13a trans-cleavage activity. *Anal. Chem.* **91**, 5278–5285 (2019).
13. Shinoda, H. et al. Automated amplification-free digital RNA detection platform for rapid and sensitive SARS-CoV-2 diagnosis. *Commun. Biol.* **5**, 1–8 (2022).
14. Shinoda, H. et al. Amplification-free RNA detection with CRISPR–Cas13. *Commun. Biol.* **4**, 1–7 (2021).
15. Metsky, H. C. et al. Designing sensitive viral diagnostics with machine learning. *Nat. Biotechnol.* **40**, 1123–1131 (2022).
16. Wessels, H.-H. et al. Massively parallel Cas13 screens reveal principles for guide RNA design. *Nat. Biotechnol.* **38**, 722–727 (2020).
17. Tambe, A., East-Seletsky, A., Knott, G. J., Doudna, J. A. & O'Connell, M. R. RNA binding and HEPN-nuclease activation are decoupled in CRISPR-Cas13a. *Cell Rep.* **24**, 1025–1036 (2018).
18. East-Seletsky, A., O'Connell, M. R., Burstein, D., Knott, G. J. & Doudna, J. A. RNA targeting by functionally orthogonal type VI-A CRISPR-Cas enzymes. *Mol. Cell* **66**, 373–383.e3 (2017).
19. Bar-Even, A. et al. The moderately efficient enzyme: evolutionary and physicochemical trends shaping enzyme parameters. *Biochemistry* **50**, 4402–4410 (2011).
20. Samson, R. & Deutch, J. M. Diffusion-controlled reaction rate to a buried active site. *J. Chem. Phys.* **68**, 285–290 (1978).
21. Ackerman, C. M. et al. Massively multiplexed nucleic acid detection with Cas13. *Nature* **582**, 277–282 (2020).
22. Ng, C. F. et al. LUCas: Light-Uncaged Cas13a using photocleavable interfering guide RNAs. Preprint at https://doi.org/10.64898/2026.02.02.700737 (2026).
23. Wang, R. et al. Genetic screens identify host factors for SARS-CoV-2 and common cold coronaviruses. *Cell* **184**, 106–119.e14 (2021).
24. Amen, A. M. et al. Blueprint for a pop-up SARS-CoV-2 testing lab. *Nat. Biotechnol.* **38**, 791–797 (2020).
25. Slaymaker, I. M. et al. High-resolution structure of Cas13b and biochemical characterization of RNA targeting and cleavage. *Cell Rep.* **26**, 3741–3751.e5 (2019).
26. Min, W. et al. Fluctuating enzymes: lessons from single-molecule studies. *Acc. Chem. Res.* **38**, 923–931 (2005).
27. Liu, L. et al. The molecular architecture for RNA-guided RNA cleavage by Cas13a. *Cell* **170**, 714–726.e10 (2017).
28. Bienert, S. et al. The SWISS-MODEL Repository—new features and functionality. *Nucleic Acids Res.* **45**, D313–D319 (2017).
29. Waterhouse, A. et al. SWISS-MODEL: homology modelling of protein structures and complexes. *Nucleic Acids Res.* **46**, W296–W303 (2018).
30. Sinha, S. et al. Unveiling the RNA-mediated allosteric activation discloses functional hotspots in CRISPR-Cas13a. *Nucleic Acids Res.* **52**, 906–920 (2024).
31. Abraham, M. et al. GROMACS 2024.1 Manual. *Zenodo* https://doi.org/10.5281/zenodo.10721192 (2024).
32. Maier, J. A. et al. ff14SB: improving the accuracy of protein side chain and backbone parameters from ff99SB. *J. Chem. Theory Comput.* **11**, 3696–3713 (2015).
33. Banáš, P. et al. Performance of molecular mechanics force fields for RNA simulations: stability of UUCG and GNRA hairpins. *J. Chem. Theory Comput.* **6**, 3836–3849 (2010).
34. Zgarbová, M. et al. Refinement of the Cornell et al. nucleic acids force field based on reference quantum chemical calculations of glycosidic torsion profiles. *J. Chem. Theory Comput.* **7**, 2886–2902 (2011).
35. Zgarbová, M. et al. Refinement of the sugar-phosphate backbone torsion beta for AMBER force fields improves the description of Z- and B-DNA. *J. Chem. Theory Comput.* **11**, 5723–5736 (2015).
36. Krepl, M. et al. Reference simulations of noncanonical nucleic acids with different χ variants of the AMBER force field: quadruplex DNA, quadruplex RNA and Z-DNA. *J. Chem. Theory Comput.* **8**, 2506–2520 (2012).
37. Zgarbová, M. et al. Toward improved description of DNA backbone: revisiting epsilon and zeta torsion force field parameters. *J. Chem. Theory Comput.* **9**, 2339–2354 (2013).
38. Jorgensen, W. L., Chandrasekhar, J., Madura, J. D., Impey, R. W. & Klein, M. L. Comparison of simple potential functions for simulating liquid water. *J. Chem. Phys.* **79**, 926–935 (1983).

Acknowledgements

We thank all members of the Fletcher, Ott and Doudna laboratories for helpful discussions and feedback on this project. We also thank S. Wyman, E. Moehle and B. Bach for providing samples from the Innovative Genomics Institute, and C. Langelier for providing samples from the Chan Zuckerberg Biohub. Purified LbuCas13a was a kind gift from Shanghai ChemPartner, and we thank Synthego for support with synthetic crRNAs. We gratefully acknowledge support from NIH/NIAID grant 5R61AI140465-03 to J.A.D., D.A.F. and M.O. and a generous gift from an anonymous donor in support of the ANCeR diagnostics consortium, as well as generous individual donors to the Gladstone Institutes. This work was supported in part by the Health Tech CoLab at the Blum Center for Developing Economies at UC Berkeley. S.S. acknowledges support from the KAIST Startup Fund. G.J.K. was supported by the Snow Medical Research Foundation (SMRF2021-276) and an NHMRC Investigator Grant (EL1, APP1175568). J.A.D. is an HHMI investigator. D.A.F. and M.O. are Chan Zuckerberg Biohub investigators. The following reagents were deposited by the Centers for Disease Control and Prevention and obtained through BEI Resources, NIAID, NIH: Genomic RNA from SARS-Related Coronavirus 2, Isolate USA-WA1/2020, NR-52285; SARS-Related Coronavirus 2, Isolate USA-WA1/2020, NR-52281; SARS-Related Coronavirus 2, Isolate hCoV-19/USA/MD-HP05285/2021 (Lineage B.1.617.2; Delta Variant), NR-56127; and Human Coronavirus, NL63, NR-470. M.O. received support from the James B. Pendleton Charitable Trust, Hellmann Foundation and P. and E. Taft. M.O. is a Nick and Sue Hellmann Distinguished Professor. T.Y.L. is supported by generous startup funds from Rutgers University-New Brunswick. This research used the Savio computational cluster resource provided by the Berkeley Research Computing program at the University of California, Berkeley (supported by the UC Berkeley Chancellor, Vice Chancellor for Research and Chief Information Officer).

Author contributions

S.S., D.A.F. and M.O. conceived and designed the study. S.S., A.L. and C.F.N. performed the experiments and S.S. analysed the data. J.S., S.I.S., P.F., G.R.K. and G.J.K. designed the crRNAs. D.B. and C.S. assisted with the BSL-3 work. J.S., S.I.S., P.F., G.R.K., G.J.K., D.C.J.S., T.Y.L. and

J.A.D. provided the reagents. G.R.K., J.A.D. and M.O. obtained the clinical samples. G.J.K., T.Y.L. and J.A.D. provided critical expertise and feedback. A.D. performed the molecular dynamics simulations. D.A.F. and M.O. supervised the study design and data collection. J.A.D., M.O. and D.A.F. secured funding. S.S. and D.A.F. wrote the paper, and all authors contributed feedback.

Competing interests

S.S., D.A.F. and M.O. have filed a patent application related to this work. The Regents of the University of California have patents issued and pending for CRISPR technologies on which J.A.D. is an inventor. J.A.D. is a co-founder of Caribou Biosciences, Editas Medicine, Scribe Therapeutics, Intellia Therapeutics and Mammoth Biosciences. J.A.D. is a scientific advisory board member of Caribou Biosciences, Intellia Therapeutics, eFFECTOR Therapeutics, Scribe Therapeutics, Mammoth Biosciences, Synthego, Algen Biotechnologies, Felix Biosciences and Inari. J.A.D. is a director at Johnson & Johnson and has research projects sponsored by Biogen, Pfizer, Apple Tree Partners and Roche. M.O. and D.A.F are cofounders of DirectBio, Inc. M.O. and J.A.D. are on the scientific advisory board for Invisishield Technologies Ltd.

Additional information

Extended data is available for this paper at https://doi.org/10.1038/s41551-026-01642-6.

Supplementary information The online version contains supplementary material available at https://doi.org/10.1038/s41551-026-01642-6.

Correspondence and requests for materials should be addressed to Sungmin Son, Melanie Ott or Daniel A. Fletcher.

Peer review information *Nature Biomedical Engineering* thanks the anonymous reviewers for their contribution to the peer review of this work.

Reprints and permissions information is available at www.nature.com/reprints.

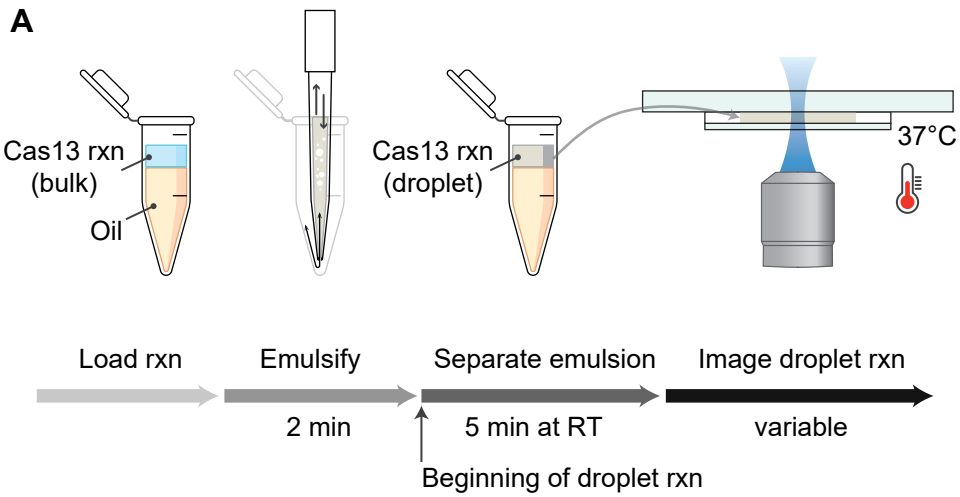
Publisher's note Springer Nature remains neutral with regard to jurisdictional claims in published maps and institutional affiliations.

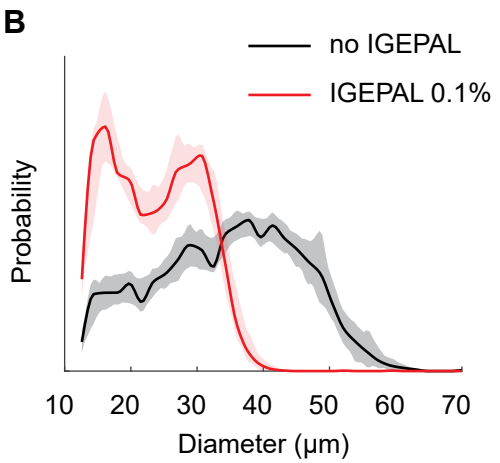
Open Access This article is licensed under a Creative Commons Attribution 4.0 International License, which permits use, sharing, adaptation, distribution and reproduction in any medium or format, as long as you give appropriate credit to the original author(s) and the source, provide a link to the Creative Commons licence, and indicate if changes were made. The images or other third party material in this article are included in the article's Creative Commons licence, unless indicated otherwise in a credit line to the material. If material is not included in the article's Creative Commons licence and your intended use is not permitted by statutory regulation or exceeds the permitted use, you will need to obtain permission directly from the copyright holder. To view a copy of this licence, visit http://creativecommons.org/licenses/by/4.0/.

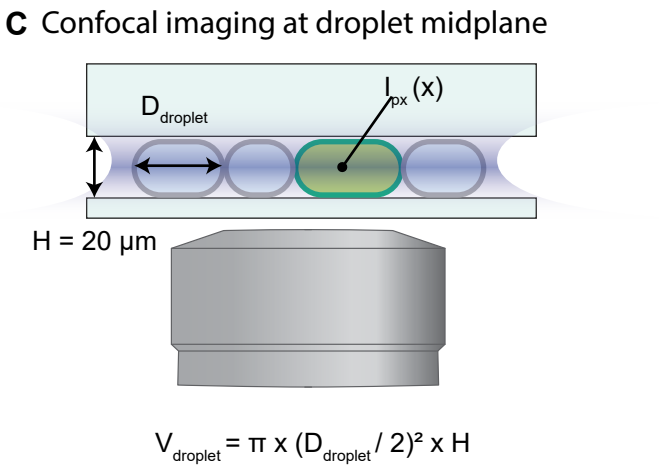
© The Author(s) 2026

[1]Department of Bioengineering, University of California, Berkeley, CA, USA. [2]Department of Bio and Brain Engineering, KAIST, Daejeon, Republic of Korea. [3]UC Berkeley–UC San Francisco Graduate Program in Bioengineering, University of California, Berkeley, CA, USA. [4]Gladstone Infectious Disease Institute, Gladstone Institutes, San Francisco, CA, USA. [5]Medical Scientist Training Program, University of California, San Francisco, San Francisco, CA, USA. [6]Biomedical Sciences Graduate Program, University of California, San Francisco, San Francisco, CA, USA. [7]Department of Medicine, University of California, San Francisco, San Francisco, CA, USA. [8]Department of Molecular and Cell Biology, University of California, Berkeley, CA, USA. [9]Innovative Genomics Institute, University of California, Berkeley, CA, USA. [10]Department of Biochemistry and Molecular Biology, Infection Program, Biomedicine Discovery Institute, Monash University, Clayton, Victoria, Australia. [11]Department of Molecular Biology and Biochemistry, Rutgers, The State University of New Jersey, Piscataway, NJ, USA. [12]Center for Advanced Biotechnology and Medicine, Rutgers, The State University of New Jersey, Piscataway, NJ, USA. [13]Molecular Biophysics and Integrated Bioimaging Division, Lawrence Berkeley National Laboratory, Berkeley, CA, USA. [14]Howard Hughes Medical Institute, University of California, Berkeley, CA, USA. [15]Department of Chemistry, University of California, Berkeley, CA, USA. [16]California Institute for Quantitative Biosciences (QB3), University of California, Berkeley, CA, USA. [17]Chan Zuckerberg Biohub, San Francisco, CA, USA. [18]Division of Biological Systems and Engineering, Lawrence Berkeley National Laboratory, Berkeley, CA, USA. ✉e-mail: smson@kaist.ac.kr; melanie.ott@gladstone.ucsf.edu; fletch@berkeley.edu

https://doi.org/10.1038/s41551-026-01642-6

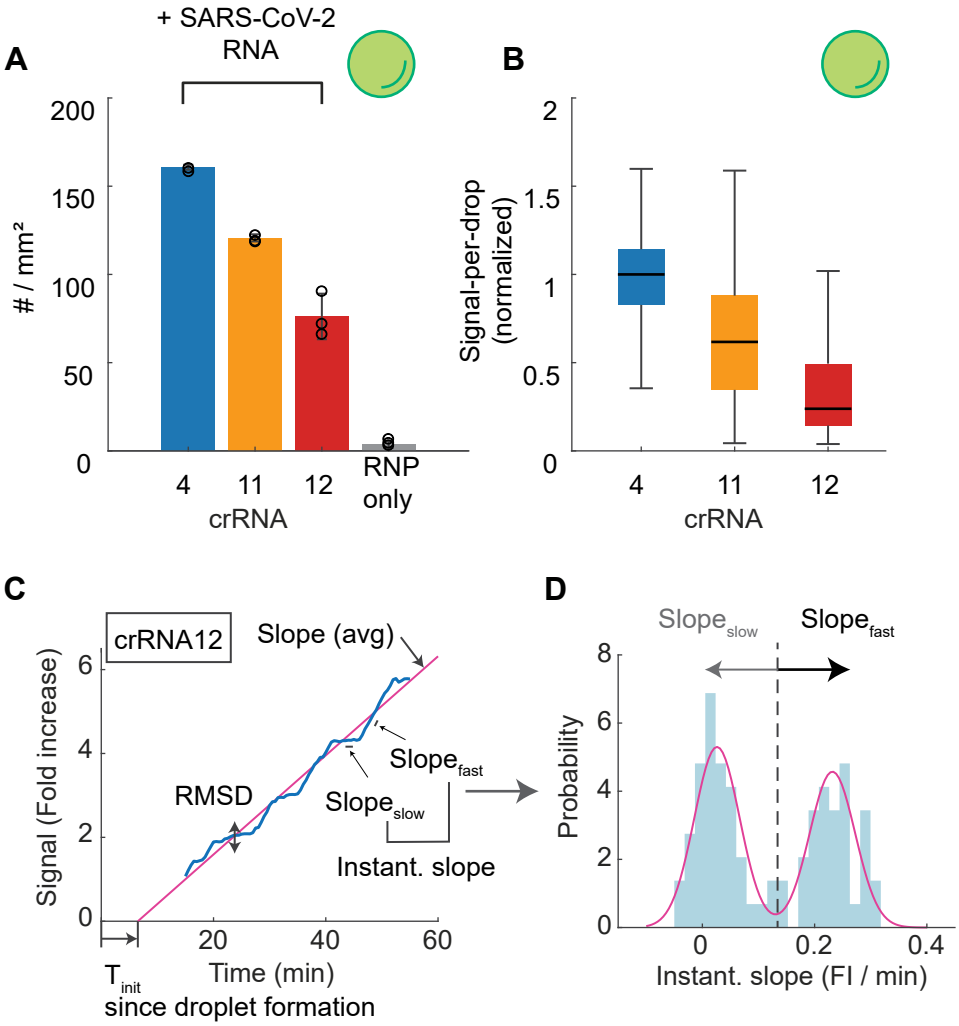






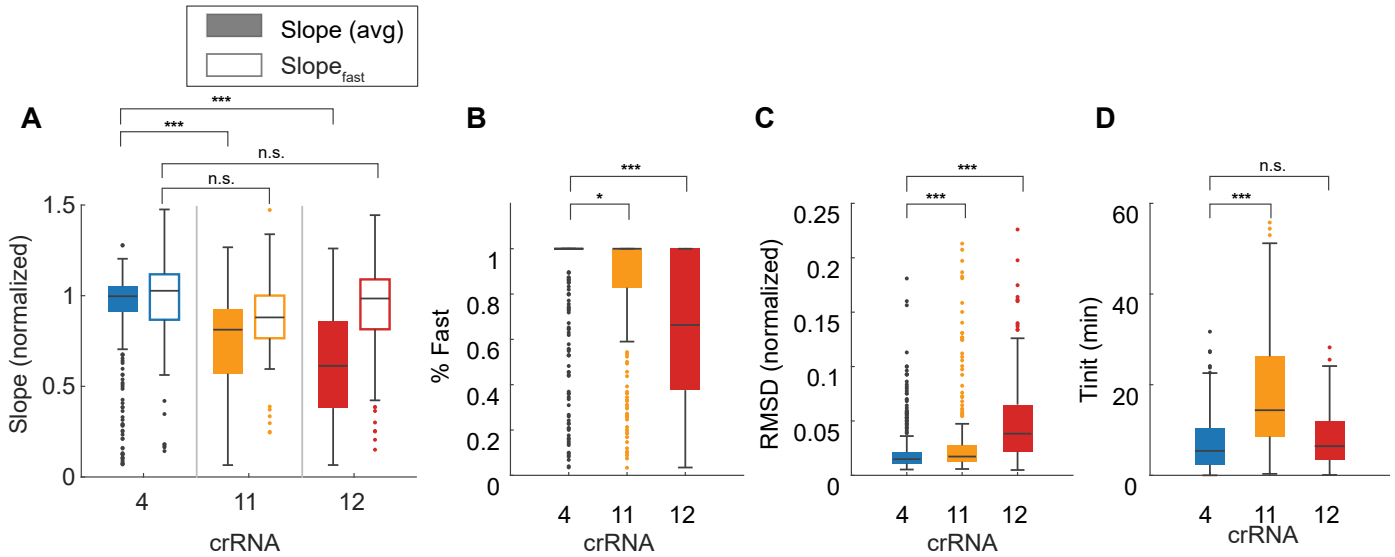
Extended Data Fig. 1 | Formation, characterization, and imaging of Cas13a reaction droplets. a) Workflow of the droplet Cas13a assay. A Cas13a reaction including target RNAs is mixed with an oil (HFE 7500 including 2% w/w Perfluoro-PEG surfactant) and emulsified by repeated pipette mixing at a constant speed for 2 minutes. The emulsified reaction is held at room temperature for 5 minutes to wait for the emulsion to be separated from the aqueous phase. Subsequently, the emulsion is loaded into a custom imaging chamber and imaged with a fluorescence microscope. **b**) Droplets containing the Cas13a reactions range in size from approximately 15 to 40 μm. The droplet size distribution (red line) is increased when the 0.1% wt/vol IGEPAL is removed from the Cas13a mix (black line). The shadows indicate the S.D. from 5 independent droplet preparations. **c**) Schematic depicting the geometry of flow cell and droplets, and confocal imaging of fluorescence signal (not drawn to scale). A 20X Water Immersion objective was used when droplet volume needed to be accurately determined. $D_{droplet}$ = droplet diameter, $V_{droplet}$ = droplet volume, $I_{px}(x)$ = fluorescence signal intensity of camera pixel in location x. Droplets larger than 20 μm deform to disks.

https://doi.org/10.1038/s41551-026-01642-6



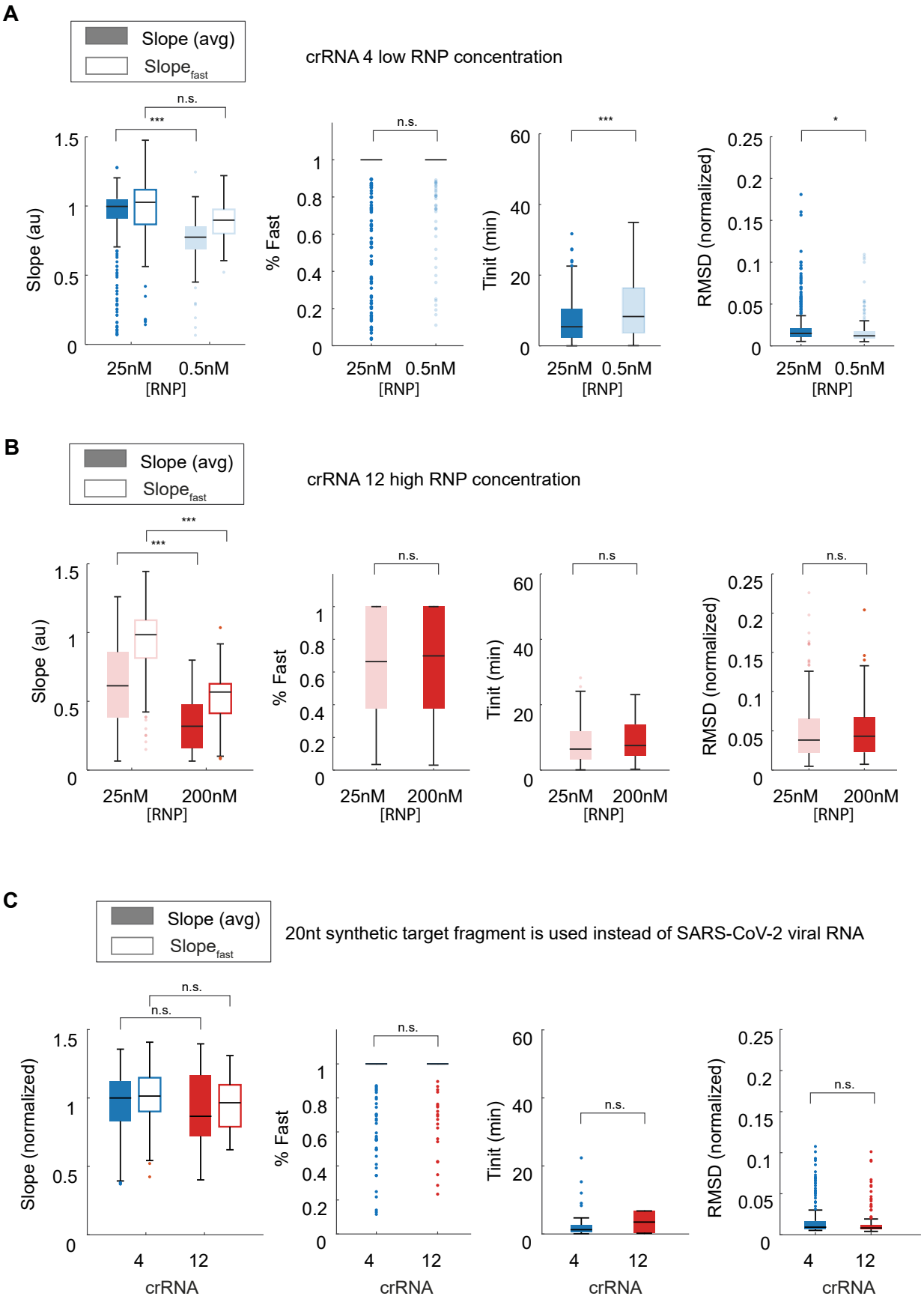
Extended Data Fig. 2 | Single-droplet Cas13a kinetics vary across crRNA–target pairs. a) The results of droplet Cas13a reactions (# positive droplets / mm^2) with 3.5 ×104 copies/µL of SARS-CoV-2 RNA for crRNAs 4, 11, and 12 after 30 minutes of incubation. The RNP only condition is measured with all three crRNAs. A total of 1287, 966, 605, and 21 positive droplets were quantified from each reaction. Data are represented as mean ± SD of three replicates except for crRNA 4, where two replicate experiments were performed. **b**) The same experiment as described in a) but reporting the average fluorescence signal in each droplet containing the different crRNAs after 30 minutes. The signal per droplet is represented as a box and whisker plot showing the median, lower and upper quartiles, and minimum and the maximum values ignoring outliers. The signal is normalized by the median of crRNA 4. **c**) Analysis strategy of an individual Cas13a signal trajectory, using crRNA 12 as an example trajectory (blue curve). The average slope (Slope (avg)) (red curve), T_{init}, and the Root-mean-square-deviation (RMSD) are determined by performing simple linear regression to the raw signal. $Slope_{fast}$ and $Slope_{slow}$ correspond to the fast and slow periods determined in d). **d**) Instantaneous slopes of the Cas13a signal trajectories are calculated by taking the time-derivative of the raw signal (blue histogram) and fitting its probability distribution with either single- or binary-Gaussian (red line). For data that favors binary distribution, we determined $Slope_{fast}$, $Slope_{slow}$, % Fast, and % Slow by taking the mean and the proportion of each Gaussian.

https://doi.org/10.1038/s41551-026-01642-6



Extended Data Fig. 3 | Quantitative analysis of single-droplet kinetic distributions. a) The distribution of slopes is represented as a box and whisker plot showing the median, lower and upper quartiles, and the 5th and 95th percentile values, with outliers overlaid as individual data points. Individual 30-minute-long trajectories from droplets of arbitrary diameter are used after their signal is normalized for droplet size. To calculate the distributions, 395, 267, and 311 trajectories are used for crRNA 4, crRNA 11, and crRNA 12, respectively. P-values determined from a two-tailed *Student's* t-test are 2.1e-20, 7.1e-45, 0.34, 0.39. ns = not significant, *p < 0.05, ***p < 0.001. **b**) The same experiment as described in a), but for % fast. P-values determined from a two-tailed *Student's* t-test are 0.021 and 4.3e-34. **c**) The same experiment as described in a), but for RMSD. P-values determined from a two-tailed *Student's* t-test are 1.5e-4 and 4.4e-30. **d**) The same experiment as described in a), but for T_{init}. P-values determined from a two-tailed *Student's* t-test are 1.6e-23 and 7.7e-2. Bulk Cas13a reaction rate for 4 ×105 copies/µL of *in-vitro* transcribed (IVT) N gene RNA was measured with crRNA 2 or 4 and represented as mean ± SD of three replicates.

https://doi.org/10.1038/s41551-026-01642-6

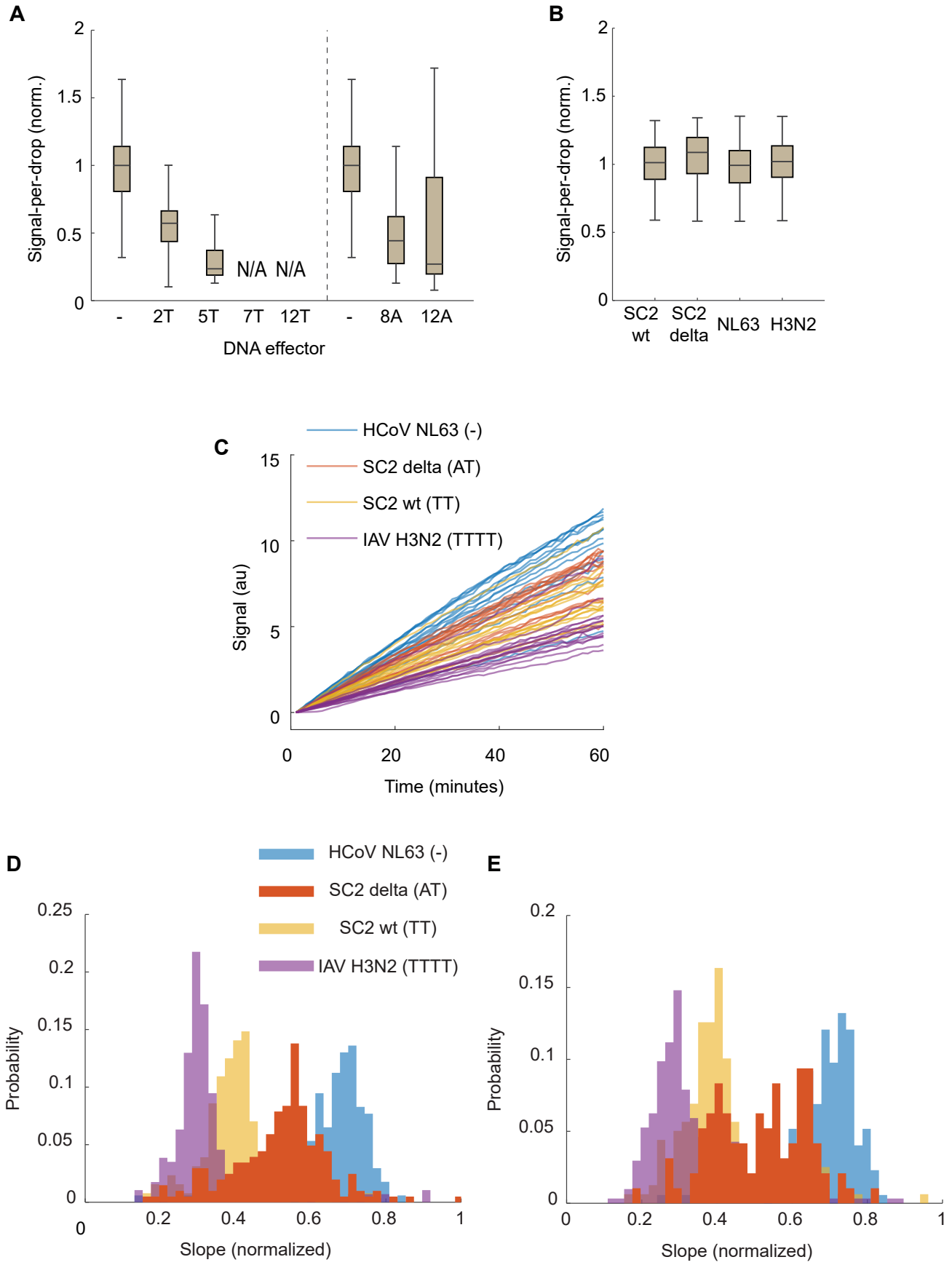


Extended Data Fig. 4 | See next page for caption.

https://doi.org/10.1038/s41551-026-01642-6

Extended Data Fig. 4 | Effects of enzyme and target concentrations on Cas13a reaction kinetics. a) Effect of RNP concentration on Cas13a reaction kinetics using crRNA 4. The distribution of slopes is represented as a box and whisker plot showing the median, lower and upper quartiles, and the 5th and 95th percentile values, with outliers overlaid as individual data points. 395 and 190 individual 30-minutes-long trajectories are collected from two replicate experiments for each RNP concentrations. P-values determined from a two-tailed *Student's* t-test are 8.8e-18 and 0.13 (slope), 0.37 (% Fast), 9.2e-5 (T_{init}), and 1.1e-2 (RMSD). ns = not significant, *p < 0.05, ** p < 0.005, ***p < 0.001. Data are represented as mean ± SD of three replicates. **b**) As in a), but for crRNA 12. We collected 311 and 102 individual trajectories from two replicate experiments for each RNP concentration. P-values determined from a two-tailed *Student's* t-test are 1.4e-17 and 6.1e-29 (slope), 0.69 (% Fast), 0.39 (T_{init}), and 0.81 (RMSD). ns = not significant, *p < 0.05, ** p < 0.005, ***p < 0.001. **c**) Effect of target RNA size on Cas13a reaction kinetics. Distribution of key parameters is represented as the box and whisker plots representing the median, the lower and upper quartiles, and the 5th and 95th percentile values, with outliers overlaid as individual data points. We collected 230 and 129 individual 30-minutes-long trajectories from two replicate experiments for each crRNA. P-values determined from a two-tailed *Student's* t-test are 0.35 and 0.34 (slope), 0.61 (% Fast), 0.21 (RMSD), and 0.91 (T_{init}). ns = not significant.

https://doi.org/10.1038/s41551-026-01642-6

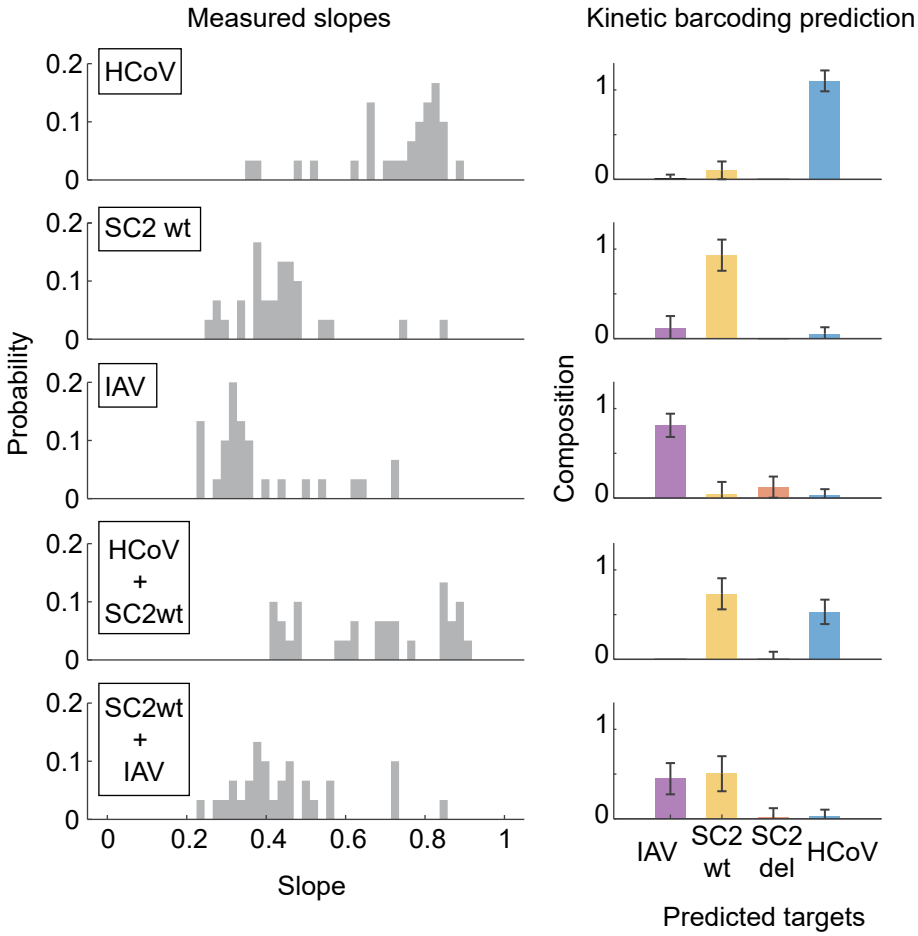


Extended Data Fig. 5 | See next page for caption.

https://doi.org/10.1038/s41551-026-01642-6

Extended Data Fig. 5 | igRNAs alter single-Cas13a activity. a) Effect of DNA effector on the droplet signal represented as a box and whisker plot showing the median, lower and upper quartiles, and the 5th and 95th percentile values ignoring outliers. All DNA modifications are made to the same crRNA (crRNA 4) and, for each crRNA design, droplet signal from SARS-CoV-2 RNA is quantified from individual droplets at the assay endpoint. N = 1525 (-), 1114 (2 T), 942 (5 T), 1368 (8 A), 484 (12 A). No positive droplets are detected for crRNAs modified with 7 T and 12 T. **b**) Droplet signal of different viruses measured with unmodified crRNAs represented as a box and whisker plot showing the median, lower and upper quartiles, and the 5th and 95th percentile values ignoring outliers. N = 263 (SARS-CoV-2 (SC2) wt), 226 (SC2 delta), 1119 (NL63), and 553 (H3N2). **c**) Raw signal time-trajectories are shown for four DNA-modified crRNAs targeting HCoV NL63, SC2 wt, SC2 delta, and IAV H3N2. The signal is normalized for droplet size and its initial value is fixed as 0. 15 representative trajectories are shown for each virus. **d**) Histogram showing the signal slope distribution of an individual virus measured with the single crRNA. **e**) Histogram showing the signal slope distribution of an individual virus measured with 4-crRNA combinations.

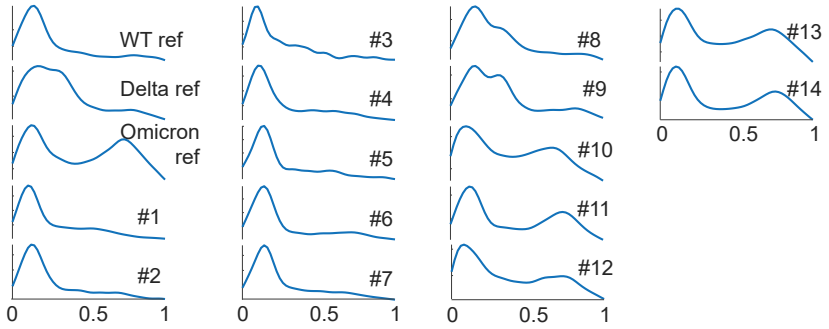
https://doi.org/10.1038/s41551-026-01642-6



Extended Data Fig. 6 | Kinetic barcoding enables multi-virus identification by slope distributions. Prediction of target viruses based on the signal slope distribution. Total 268, 272, 518, 157, 119 trajectories were obtained for HCoV, SC2 wt, IAV, HCoV+SC2wt, and SC2wt+IAV, respectively. Among those, 30 trajectories are randomly selected from each sample (representative distribution shown on the left) and the target virus compositions are predicted from the subset. The bar graph on the right shows the mean and standard distribution of target predictions from 100 repeated sampling

https://doi.org/10.1038/s41551-026-01642-6

A



B

Sample #	Ct	Sample	Difference (Kernel)			Difference (K-S)			Prediction
			WT	Delta	Omicron	WT	Delta	Omicron	
WT ref	N/A	WT	0.0000	0.0115	0.0148	1.00E+00	1.29E-37	9.75E-76	WT
Delta ref	N/A	Delta	0.0115	0.0000	0.0130	1.29E-37	1.00E+00	5.15E-93	Delta
Omicron ref	N/A	Omicron	0.0148	0.0130	0.0000	9.75E-76	5.15E-93	1.00E+00	Omicron
1	15.9	WT	0.0065	0.0138	0.0157	3.51E-10	2.83E-111	1.61E-162	WT
2	16.9	WT	0.0027	0.0126	0.0156	1.06E-01	1.21E-31	1.75E-61	WT
3	15.9	WT	0.0086	0.0142	0.0182	5.07E-02	4.18E-04	2.90E-07	WT
4	15.9	WT	0.0052	0.0137	0.0152	3.58E-04	2.13E-47	1.60E-71	WT
5	13.4	WT	0.0043	0.0140	0.0168	2.83E-01	1.39E-18	9.77E-29	WT
6	14.6	WT	0.0039	0.0146	0.0164	1.65E-03	1.08E-65	1.72E-112	WT
7	16.4	WT	0.0030	0.0116	0.0148	1.47E-02	1.82E-55	1.58E-114	WT
8	N/A	Delta	0.0089	0.0033	0.0125	3.85E-27	3.26E-03	3.13E-99	Delta
9	N/A	Delta	0.0112	0.0018	0.0128	2.09E-30	4.97E-01	1.55E-69	Delta
10	19.4	Omicron	0.0135	0.0107	0.0046	2.82E-76	4.73E-82	9.54E-20	Omicron
11	19.7	Omicron	0.0113	0.0123	0.0042	5.38E-57	3.09E-77	1.22E-14	Omicron
12	19.7	Omicron	0.0113	0.0104	0.0057	2.60E-40	1.74E-40	9.31E-22	Omicron
13	19.3	Omicron	0.0139	0.0122	0.0019	1.11E-93	1.27E-123	4.25E-03	Omicron
14	18.6	Omicron	0.0124	0.0131	0.0038	6.03E-76	1.19E-106	4.05E-11	Omicron

Extended Data Fig. 7 | Clinical validation of kinetic barcoding across patient samples. a) Kernel function of all samples measured at assay endpoint. **b**) Clinical sample information and the difference between the clinical sample versus the standard curves as determined by RMSE or the Kolmogorov–Smirnov test. The grey shading indicates incorrect predictions.

nature portfolio

Corresponding author(s): Daniel A. Fletcher

Last updated by author(s): Nov 21, 2025

Reporting Summary

Nature Portfolio wishes to improve the reproducibility of the work that we publish. This form provides structure for consistency and transparency in reporting. For further information on Nature Portfolio policies, see our Editorial Policies and the Editorial Policy Checklist.

Statistics

For all statistical analyses, confirm that the following items are present in the figure legend, table legend, main text, or Methods section.

n/a	Confirmed	
☐	☒	The exact sample size (*n*) for each experimental group/condition, given as a discrete number and unit of measurement
☐	☒	A statement on whether measurements were taken from distinct samples or whether the same sample was measured repeatedly
☐	☒	The statistical test(s) used AND whether they are one- or two-sided *Only common tests should be described solely by name; describe more complex techniques in the Methods section.*
☒	☐	A description of all covariates tested
☐	☒	A description of any assumptions or corrections, such as tests of normality and adjustment for multiple comparisons
☐	☒	A full description of the statistical parameters including central tendency (e.g. means) or other basic estimates (e.g. regression coefficient) AND variation (e.g. standard deviation) or associated estimates of uncertainty (e.g. confidence intervals)
☐	☒	For null hypothesis testing, the test statistic (e.g. *F*, *t*, *r*) with confidence intervals, effect sizes, degrees of freedom and *P* value noted *Give P values as exact values whenever suitable.*
☒	☐	For Bayesian analysis, information on the choice of priors and Markov chain Monte Carlo settings
☒	☐	For hierarchical and complex designs, identification of the appropriate level for tests and full reporting of outcomes
☒	☐	Estimates of effect sizes (e.g. Cohen's *d*, Pearson's *r*), indicating how they were calculated

Our web collection on statistics for biologists contains articles on many of the points above.

Software and code

Policy information about availability of computer code

Data collection	All microscopy images are collected using Nikon Elements and Micro-Manager 1.4. Bulk Cas13 reaction are performed using a plate reader (TECAN, infinite 200Pro) and data were exported to Microsoft Excel.
Data analysis	All image analyses were performed in MATLAB R2020b using the procedures described in the Methods section.

For manuscripts utilizing custom algorithms or software that are central to the research but not yet described in published literature, software must be made available to editors and reviewers. We strongly encourage code deposition in a community repository (e.g. GitHub). See the Nature Portfolio guidelines for submitting code & software for further information.

Data

Policy information about availability of data

All manuscripts must include a data availability statement. This statement should provide the following information, where applicable:

- Accession codes, unique identifiers, or web links for publicly available datasets
- A description of any restrictions on data availability
- For clinical datasets or third party data, please ensure that the statement adheres to our policy

All data supporting the findings of this study are provided in the Source Data files. The oligonucleotide sequences are described in Supplementary Table 1. The plasmid used to express MBP-tagged LbuCas13a (p2CT-His-MBP-Lbu_C2c2_WT) is available from Addgene (83482)

Research involving human participants, their data, or biological material

Policy information about studies with human participants or human data. See also policy information about sex, gender (identity/presentation), and sexual orientation and race, ethnicity and racism.

Reporting on sex and gender	This study procedures were limited to secondary data analysis of non-identifiable biospecimens, for which there was no link to identifiable subject information.
Reporting on race, ethnicity, or other socially relevant groupings	This study procedures were limited to secondary data analysis of non-identifiable biospecimens, for which there was no link to identifiable subject information.
Population characteristics	This study procedures were limited to secondary data analysis of non-identifiable biospecimens, for which there was no link to identifiable subject information.
Recruitment	This study procedures were limited to secondary data analysis of non-identifiable biospecimens, for which there was no link to identifiable subject information.
Ethics oversight	This study procedures were limited to secondary data analysis of non-identifiable biospecimens, for which there was no link to identifiable subject information.

Note that full information on the approval of the study protocol must also be provided in the manuscript.

Field-specific reporting

Please select the one below that is the best fit for your research. If you are not sure, read the appropriate sections before making your selection.

☒ Life sciences ☐ Behavioural & social sciences ☐ Ecological, evolutionary & environmental sciences

For a reference copy of the document with all sections, see nature.com/documents/nr-reporting-summary-flat.pdf

Life sciences study design

All studies must disclose on these points even when the disclosure is negative.

Sample size	No sample size calculations were performed. The number of clinical samples was limited by the number and volume of individual samples obtained from the IGI testing lab. For individual Cas13 reactions using a patient sample, we used the RNA volume of <1uL since most of the patient RNA samples were available in low volumes (< 3uL). For reactions using an IVT or cultured virus RNA, we also used <1uL RNA for consistency of the assay. For the limit of detection study, ~20% of sample was measured (i.e. a total 3.4uL of the 20uL sample was imaged with a 4X objective) to maximize the assay throughput without reducing the sensitivity. For the kinetics measurements, more than 100 individual 30-minutes-long trajectories were collected to enable statistical comparisons between conditions.
Data exclusions	No data were excluded from the analysis. During the analysis, we selected positive droplets by applying a threshold based on the circularity and total fluorescence signal of a droplet. We used the same threshold throughout the study.
Replication	All measurements were replicated two or three times as indicated in the figures.
Randomization	No randomization of patient samples was performed due to the limited availability. For IVT, cultured virus RNA, or synthetic RNA targets, Sample and control reactions for biochemical experiments were assembled with the same reagents and volumes, and were measured at the same time in the plate reader or compact detector when making direct comparisons to a control.
Blinding	The sequence information of patient samples was known at the time of measurement but it did not affect the assay or statistical analyses. No blinding was performed for other samples (e.g. IVT, cultured virus RNA, synthetic RNA targets), as it was necessary to know which reaction had target RNA and which reactions contained controls in order to set up the reactions testing the detection sensitivity, speed, and accuracy of our assay.

Reporting for specific materials, systems and methods

We require information from authors about some types of materials, experimental systems and methods used in many studies. Here, indicate whether each material, system or method listed is relevant to your study. If you are not sure if a list item applies to your research, read the appropriate section before selecting a response.

Materials & experimental systems

n/a	Involved in the study
☒	☐ Antibodies
☐	☒ Eukaryotic cell lines
☒	☐ Palaeontology and archaeology
☒	☐ Animals and other organisms
☒	☐ Clinical data
☒	☐ Dual use research of concern
☒	☐ Plants

Methods

n/a	Involved in the study
☒	☐ ChIP-seq
☒	☐ Flow cytometry
☒	☐ MRI-based neuroimaging

Eukaryotic cell lines

Policy information about cell lines and Sex and Gender in Research

Cell line source(s)	Vero CCL-81 cells (Monkey origin) were obtained from ATCC. The Huh7.5.1-ACE2 cells were obtained from Andreas Puschnik (Wang et al, 2021)
Authentication	The Vero CCL-81 cells can be authenticated by ATCC. The Huh7.5.1-ACE2 cells were not authenticated for this study.
Mycoplasma contamination	All cell lines tested negative for mycoplasma contamination.
Commonly misidentified lines (See ICLAC register)	No cell lines commonly misidentified per ICLAC register were used.

Plants

Seed stocks	N/A
Novel plant genotypes	N/A
Authentication	N/A